Assessing permafrost erosion in the Canadian Beaufort Sea, Herschel Island – a biomarker approach

Master Thesis M.Sc. Marine Geoscience

Submitted by: Thorsten Riedel

Matriculation number: 2989087

Bremen, 18.05.2017

Supervisors: Prof. Dr. Gesine Mollenhauer

Dr. Enno Schefuß

Content

List of tables

List of figures

Abstract

Herschel Island is the remnant of an ice-push moraine, formed during the farthest advance of the Laurentide Ice Sheet in the late Wisconsin. The island is located in the Canadian Beaufort Sea, in the northwestern part of the Yukon Territory. A marine depression (Herschel Basin), southeastern adjacent to Herschel Island, acts as a sink of organic matter (OM) derived from various sources.

The main objective of this master thesis was to determine the amount of OM, derived from Herschel Island, in the deposits of Herschel Basin. Rapidly increasing mean annual air temperatures (MAAT) in high latitude areas raise awareness of a changing Arctic climate and consequences for the Arctic carbon cycle.

Biomarker analyses of soil and sediment samples from various study sites on and around Herschel Island show that sediments in Herschel Basin are of prevailing terrigenous origin. Approximately 60 % of the OM in the surface sediments of Herschel Basin and the adjacent nearshore area can be assigned to eroded material from Herschel Island. Investigations on a sediment core from the centre of the basin suggest enhanced erosion rates and increased supply by OM from Herschel Island in the upper section of the core.

Results of biomarker analyses of this thesis corroborate a progressing change of the Arctic climate, amplified by positive carbon feedback mechanisms.

Statement of authorship

_____
Name

Declaration acc.to § 10 Paragraph 11 Common Part of the Master Examination Regulations

I hereby declare that I wrote this master thesis independently and that I did not use other sources and auxiliary means than the ones indicated.

This master thesis has not been submitted in another examining procedure.

I further declare that the master thesis will not be made available to the public in this version.

Place/Date: _____

Signature: _____

1.   Introduction

1.1.   Permafrost erosion in nearshore Arctic areas

Permafrost regions of the high latitudes contain about 50 % of the global soil organic carbon pool (SOC; about 1700 Pg; Tarnocai et al., 2009). Most of this huge carbon pool, of which the majority accumulated in the Holocene and the Pleistocene (Streletskiy et al., 2014), occurs in perennially frozen permafrost deposits. Decreased decomposition rates as consequence of poor drainage and low temperatures (Davidson and Janssens, 2006) protect these deposits from large involvement in the Arctic carbon cycle.

Permafrost refers to all earth material, whether it is ice or organic material, that remains at or below 0 °C for at least two consecutive years (Brown and Kupsch, 1974; Van Everdingen, 1998). Excluding Antarctica, 17 % of the surface of the earth are affected by permafrost (Gruber, 2012). Most of the permafrost is situated in the high latitudes with only minor occurrence in alpine regions (see Fig. 1.1). According to Lantuit et al. (2012a) 34 % of the world's coastlines are affected by permafrost.

Fig. 1.1: Permafrost distribution of the circumpolar Arctic (International Permafrost Association, 1998)

Previously frozen organic carbon (OC), stored in permafrost-affected soils, can be mobilised and released into the Arctic Ocean by thawing of permafrost. Mobilised OC, now integrated in biogeochemical cycles, can be mineralised and intensify global warming by releasing greenhouse gases into the atmosphere (Gruber et al., 2004; Schuur et al., 2015). This positive carbon feedback can be attenuated by biosphere uptake of carbon (Schuur et al., 2008; Tarnocai et al., 2009), or reburial in the nearshore coastal area or off-shelf in deeper areas (Vonk and Gustafsson, 2013). The decisive question is, to what extent this carbon feedback will affect climate change (Schuur et al., 2015; Vonk and Gustafsson, 2013).
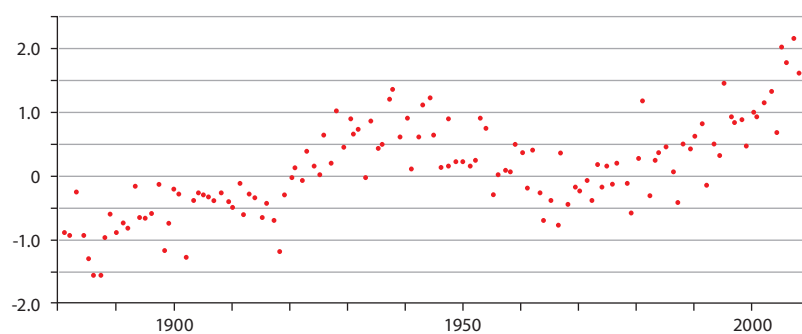
Fig. 1.2: Change of the mean air temperature (1961 – 1990, °C) recorded from land-based weather stations in the Arctic (modified after AMAP (2012))

The Arctic region is extremely sensitive to climate change. Increasing mean annual air temperatures (MAAT; Fig. 1.2) and sea temperatures will have the strongest effect in Arctic regions (Kattsov and Källén, 2005) and on its permafrost coastlines. Likewise, sea level rise in the Arctic Ocean is above average (Meehl et al., 2007).

Increasing temperatures in the Arctic result in thinning of the Arctic sea ice, earlier ice break-up and as a result lengthening of the open water season (Anisimov et al., 2007). Rising sea levels and lengthened open water seasons are expected to aggravate the intensity and frequency of storm surges, resulting in increased permafrost erosion in coastal areas (IPCC, 2007). Decrease of ground stability in permafrost regions is affecting ecosystems (IPCC, 2007), as well as industrial and municipal infrastructure in the Arctic (Fritz et al., 2017).

The most distinct temperature change occurs in the southern Beaufort Sea (Fig. 1.3). Within the last century, the MAAT increased by 2.6 °C at Herschel Island. Between 1899 and 1905 a MAAT of -12.2 °C was recorded. From 1999 to 2005 the MAAT increased to -9.6 °C (Burn and Zhang, 2009).

Herschel Island is located along the Yukon Coastal Plain (YCP; Fig. 1.3). The area is controlled by low MAAT temperatures throughout the year, resulting in formation of continuous permafrost and seasonal sea-ice for about nine months of the year (Harper, 1990). The usual thickness of permafrost on the Yukon Coastal Plain (YCP) is around 300 m (de Krom, 1990). However, permafrost thickness can exceed 600 m along the YCP (Smith and Burgess, 2000). Canadian Beaufort Sea coastlines are characterised by high average coastal erosion rates of 1.12 m/a (Lantuit et al., 2012a). The average coastline retreat on Herschel Island amounts 0.68 m/a (Obu et al., 2016). Average coastal erosion rates refer to combined aggradation and erosion (Lantuit et al., 2012a).

Mean temperature change, °C

-1.0 -0.5 0 0.5 1.0 1.5 2.0 2.5 3.0
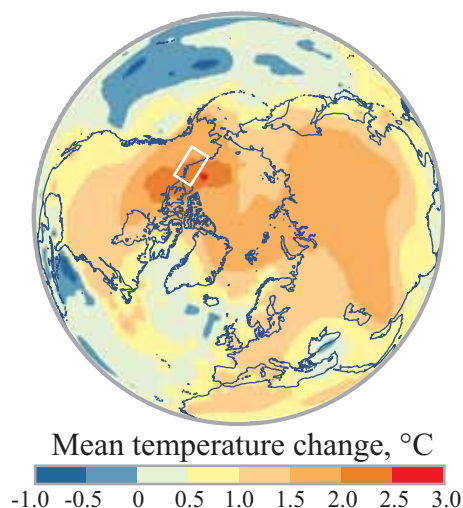
Fig. 1.3: 1957 – 2006 temperature change in the Arctic (modified after AMAP (2012)). The white rectangle depicts the location of the Yukon Coast along the southern Beaufort Sea

Coastal permafrost erosion on Herschel Island has been subject to a large number of studies (Lantuit and Pollard, 2008; Olynyk, 2008; Radosavljevic et al., 2015), concerning OC release and sediment flux in the southern Beaufort Sea, as well as threats to coastal near infrastructure in the Arctic. Yet, the fate of mobilised OC eroded from coastal deposits on Herschel Island remains widely unknown. For further understanding of the carbon complexities in the southern Beaufort Sea, investigations on possible depositional environments are necessary.

1.2. Thesis objectives

The aim of this master thesis is to distinguish between different sediment sources which influence the sedimentation in Herschel Basin. Herschel Basin is a marine depression in the southeast of Herschel Island. Furthermore, an attempt is made to quantify organic matter (OM) derived from Herschel Island in the sediments of Herschel Basin.

Sediments of Herschel Basin act as climate archives, in which changes in composition and derivation of OM is recorded. The OM associated with these deposits contains a complex mixture of biomarkers derived from a variety of aquatic and terrigenous sources (Winterfeld et al., 2015).

To distinguish between potential sources of OC, various geochemical biomarkers will be combined and compared with literature data. Consulted biomarkers are briefly summarised in paragraph 1.3. "Biomarker outline".

Prior to analyses of this thesis the following questions were developed:

1. Do potential sources of sediment input in Herschel Basin feature specific biomarker signatures?

2. Can different sources of terrestrial OC input into Herschel Basin be spatially distinguished and quantified?

3. How did coastal permafrost erosion on Herschel Island change in the past 4 ka BP?

1.3.   Biomarker outline

1.3.1.   Hopanes

Hopanes ($C_{27} - C_{35}$) are widely occurring pentacyclic triterpenes (Requejo and Halpern, 1989) synthesised from bacteriohopanetetrol. Bacteriohopanetetrol is commonly found in cell membranes of prokaryotic organisms (Requejo and Halpern, 1989). Hopanes consist of three stereoisometric series, the 17β,21β-, 17β,21α- and 17α,21β(H) configuration (Peters et al., 2005). The α and β notation indicates whether the hydrogen atoms, which are bound to the carbon skeleton of the hopanoids, are located below or above the pentacyclic ring structure (Fig. 1.4; Peters et al., 2005).

As the stereochemical arrangement of bacteriohopanetetrol is thermally labile, diagenesis and catagenesis result in transformation of the stereoisometric series as presented in Fig. 1.4.

Hopanes with the 17α,21β(H) configuration have a higher thermodynamic stability as the precedent 17β,21β(H) configuration and are therefore commonly occurring in petroleum reservoirs (Peters et al., 2005).
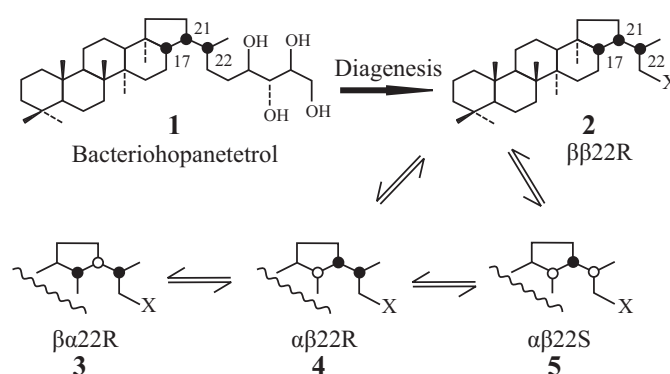
Fig. 1.4: Schematic view of the diagenetic succession of hopanes from bacteriohopanetetrol (Peters et al., 2005). The isomerization during diagenesis and catagenesis proceeds from 1 to 5 as indicated

22S and 22R homologues, as presented in Fig. 1.4 are the result of an additional asymmetric centre at the C-22 position only found in homohopanes (Peters et al., 2005). Homohopanes is the common term for hopanes with more than 30 carbon atoms.

22S and 22R configurations can be applied for assessing the biomarker maturity in oils and shales. The relative amount of the 22R configuration, found in bacteriohopanetetrol (compare Fig. 1.4), decreases with increasing burial depth up to a terminal ratio of both homologues (Abbott et al., 2001).

1.3.2.   *n*-alkanes

Saturated *n*-alkanes (normal alkanes; Chibnall et al., 1934) are straight-chain, particularly robust (Eglinton and Logan, 1991) easily identifiable hydrocarbons. *n*-alkanes occur in parts of the epicuticular leaf wax structure of terrestrial plants (Albert et al., 1934; Bush and McInerney, 2013) or are produced by microbial communities (Choi and Lee, 2013). *n*-alkanes can also occur in a variety of different settings which have been investigated in numerous studies.

The chain length of the homologue *n*-alkanes depends on the source organism and is characteristic for different environments (Castañeda and Schouten, 2011). Long-chain *n*-alkanes (n-C_{21} to n-C_{37}) are dominant in the epicuticular leaf wax of terrestrial plants with a typical distribution of odd numbered over even numbered alkanes (Eglinton and Hamilton, 1967; Bush and McInerney, 2013). In Bird et al. (1995) stable carbon isotope compositions of *n*-alkanes were used to define between different vegetation types ($C_3 - C_4$ plants). Nott et al. (2000) and Pancost et al. (2002) reported the occurrence of more intermediate *n*-alkane chain lengths observed in *Sphagnum* species from bog vegetation. In particular C_{23} and also C_{25} *n*-alkanes are reported to be characteristic for *Sphagnum* species (Nott et al., 2000; Nichols et al., 2006; Vonk and Gustafsson, 2009).

Aquatic origin of *n*-alkanes has been reported in several studies (Cranwell et al., 1987; Sachse et al., 2004). Lichtfouse et al. (1994) discusses a possible algal contribution in n-C_{25} to n-C_{35} alkanes. According to Ficken et al. (2000) n-C_{21} to n-C_{32} alkanes, produced by aquatic macrophytes, contribute to OM in lacustrine settings (see also Mead et al., 2005). Carbon Preference Index (CPI) values studied by Schefuß et al. (2003) indicate a marine derivation of the C_{24} alkane.

The chemical composition of these biomarkers is altered by biodegradation (Bost et al., 2001; Requejo and Halpern, 1989; Volkman et al., 1983) which has been mostly studied in crude oil (Bailey et al., 1973; Reed, 1977; Seifert and Moldowan, 1978; Wardroper et al., 1984) but also occurs in mature soils and sediments (Abbott et al., 2001; Peters et al., 2005).

Biodegradation occurs at temperatures up to 77 °C (Philippi, 1977) and often results in formation of unresolved complex mixtures (UCM; Fig. 1.5) (Gough et al., 1992; Nievas et al., 2008). These UCM's develop by sequential removal of *n*-alkanes and other hydrocarbons (e.g. Wenger and Isaksen (2002)).
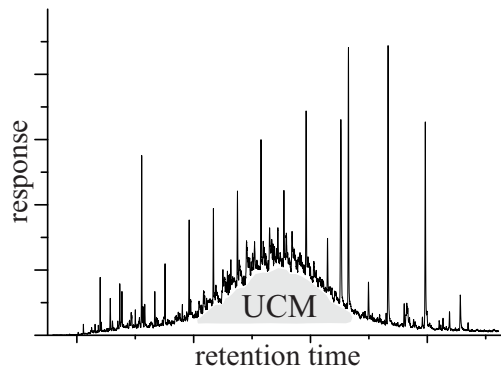
Fig. 1.5: Saturate fraction chromatogram of sample PG 2303-7/1-2, showing a distinct UCM

1.3.3.   GDGT's

Glycerol dialkyl glycerol tetraether (GDGT) lipids (Schouten et al., 2000; Schouten et al., 2013) are ubiquitously occurring membrane lipids synthesised by various archaeal and bacterial communities. Due to their occurrence in diverse environments (e.g. De Rosa and Gambacorta, 1988; Powers et al., 2004; Schouten et al., 2007b) and good preservation in immature sediments, GDGT's are commonly used to calculate paleo sea-surface temperatures (SST) (Schouten et al., 2002; Kim et al., 2012; Mollenhauer et al., 2015) and quantify terrigenous sediment input in aquatic systems (Hopmans et al., 2004).
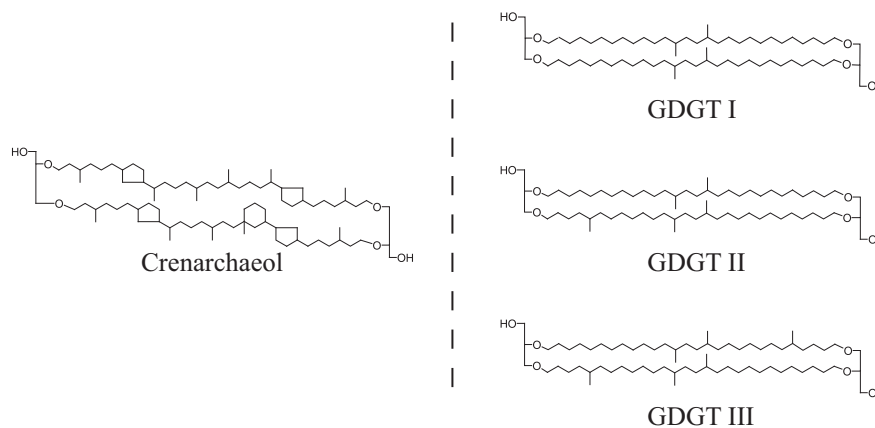
Fig. 1.6: Isoprenoidal (left) and branched (right) skeleton structures of GDGT's modified after Schouten et al. (2013)

GDGT's can be structurally divided into two groups. Isoprenoid GDGT's, for example crenarchaeol (see Fig. 1.6), consist of an isoprenoidal skeleton structure that is built from isopentyl pyrophosphate (Schouten et al., 2013).

Branched GDGT's (e.g. Fig. 1.6) (Sinninghe Damsté et al., 2000; Weijers et al., 2006b) are synthesised by bacteria and archaea and are mainly occurring in peat bogs and soils (Schouten et al., 2000; Weijers et al., 2006a). Alkyl moieties of branched GDGT's are composed of branched carbon chains instead of isoprenoid units.

2. Study area

2.1. Genesis and geological setting of Herschel Island
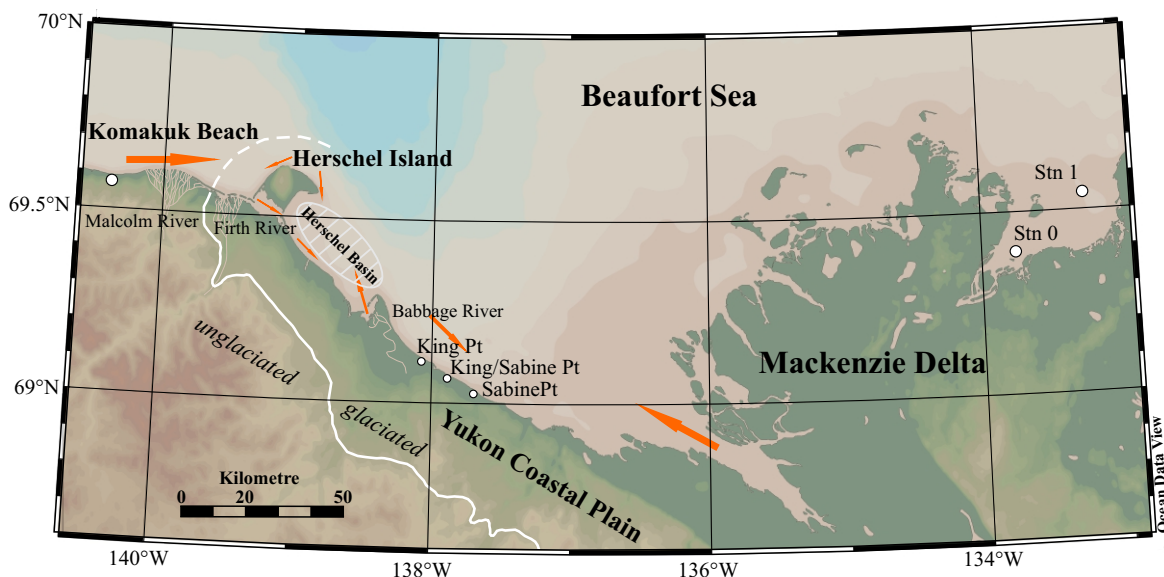
Fig. 2.1: Overview of the study area with major currents, sediment inflows (indicated by orange arrows (Pelletier et al., 1984)) and sample locations after Yunker et al. (1992). The white line (dashed and solid) indicates the farthest extent of the LIS. The YCP left of Herschel Island remained unglaciated

The study area of this thesis comprises the area around Herschel Island (69°36′N, 139°04′W) (Fig. 2.1) in the southern Canadian Beaufort Sea. Herschel Island is a remnant of the Laurentide Ice Sheet (LIS) in the eastern periphery of Beringia, marking its maximum northwestern extent in the late Wisconsin between 23 − 18 cal ka BP (Dyke and Prest, 1987; Fritz et al., 2012;

Mackay, 1959). Herschel Island has a surface area of 108 km^2 and a maximum elevation of 183 m a.s.l. (Bouchard, 1974; de Krom, 1990; Lantuit & Pollard, 2008). The island remained connected to the Yukon Coastal Plain (YCP) until it became an island approximately within the last 1.6 cal ka BP (Rampton, 1982; Burn, 2009), through sea-level changes in the Canadian Beaufort Sea (Hill et al., 1985). On present day, Herschel Island is connected to the YCP by the shallow, three kilometre wide "Workboat Passage". Westwards of Herschel Island, between Firth and Malcolm River, the YCP remained unglaciated. Mackay (1959) firstly proposed the theory that Herschel Island consists of deposits derived from Herschel Basin which origin is directly related to the ice-thrust of the LIS. This theory is supported by volumetric comparison between Herschel Island and Herschel Basin, which are of similar size. Herschel Basin is located adjacent to the southeast of Herschel Island. The basin has a maximum depth of about 70 mbsl (Fig. 2.2). Its oval shape extents in a southeast stretch parallel to the YCP and is separated by the Herschel Sill from the Mackenzie Trough (O'Connor, 1984).
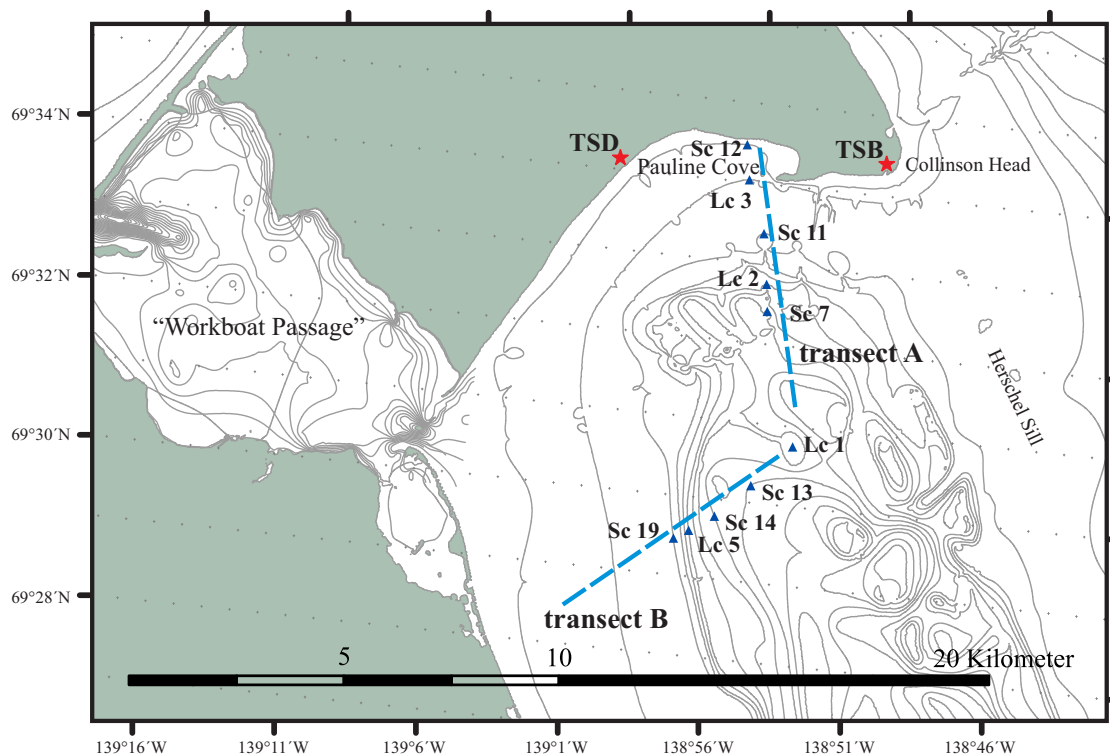
Fig. 2.2: Bathymetry of Herschel Basin with coring locations (Sc = short core; Lc = long core) along transect A and B, as well as outcrops on Herschel Island. The gap between two isobaths represents five metres

As the LIS advanced towards the YCP, it presumably thrusted over the subaerial exposed continental shelf (Mackay, 1959) and agglomerated various deposits (Bouchard, 1974). Deposits on Herschel Island indicate preglacial, glacial and postglacial origin (Fritz et al., 2012; Bouchard, 1974). Preglacial deposits are of terrestrial and marine origin and most common on Herschel Island. Through ice-thrusting during the Wisconsin glaciation, these deposits have undergone deformation and redeposition. Glacial deposits combine erratic boulders and gravel which can be found on the surface of Herschel Island. Some of these gravel deposits could be of fluvioglacial origin (Bouchard, 1974). Postglacial deposits such as peat and soil summarise sediments accumulated during pedogenesis, as well as alluvial accumulations (Bouchard, 1974).

The literature about ground-ice content on Herschel Island concludes in several statements. Pollard (1990) mentions a massive ground-ice content of up to 70 % in the upper $10 - 15$ m of the permafrost deposits. Mackay (1971) states a ground-ice content of up to 50 % in the near-surface permafrost. Most of the ground-ice on Herschel Island occurs as massive segregated ice lenses within the disturbed Pleistocene deposits (Mackay, 1971).

Massive ground-ice content in permafrost soils on Herschel Island leads to intense thermokarst activities (Lantuit and Pollard, 2005). Often initiated by coastal erosion, vast ground-ice bodies result in development of retrogressive thaw slumps (RTS) (Pollard, 1990; Lantuit & Pollard, 2008; Lantz and Kokelj, 2008). These bowl-shaped structures (Fig.2.3) show fast inland erosion and mobilization of soil in the prevailing unlithified permafrost deposits on Herschel Island (Lantuit et al., 2012b; Lantuit & Pollard, 2008; Obu et al., 2016). RTS are abundantly occurring on the southeast and northeast coast of Herschel Island (Bouchard, 1974).
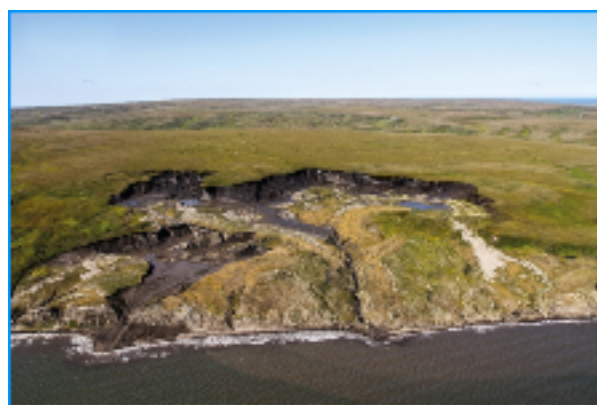
Fig. 2.3: Bowl-shaped extent of thaw slump D located at the east coast of Herschel Island (Obu et al., 2016)

2.2.   Potential sources of sediment

Approximately 130 km eastwards of Herschel Island, the Mackenzie River issues into the Beaufort Sea. With a drainage area of 1.78 x 10^6 km^2 and an annual water discharge of 316 km^3/a (Holmes et al., 2012), it is the 4th largest of the Arctic rivers. Each year the Mackenzie River discharges 2.1 Mt/a of terrestrial particulate organic carbon (POC) and 1.3 Mt/a of terrestrial dissolved organic carbon (DOC) into the Mackenzie Delta and the adjacent nearshore area (Carrie et al., 2009; Couture, 2010; Macdonald et al., 1998). Annually discharging 128 Mt of sediments (investigated from 1974 to 1994) the Mackenzie River is the largest contributor of suspended particulate matter (SPM) in the Arctic Ocean (Forbes, 1981; Hill et al., 1991; Holmes et al., 2012; Vonk et al., 2015). 124 Mt of the annual sediment flux consists of silty sediments or particles of smaller grainsize (Carson et al., 1998).
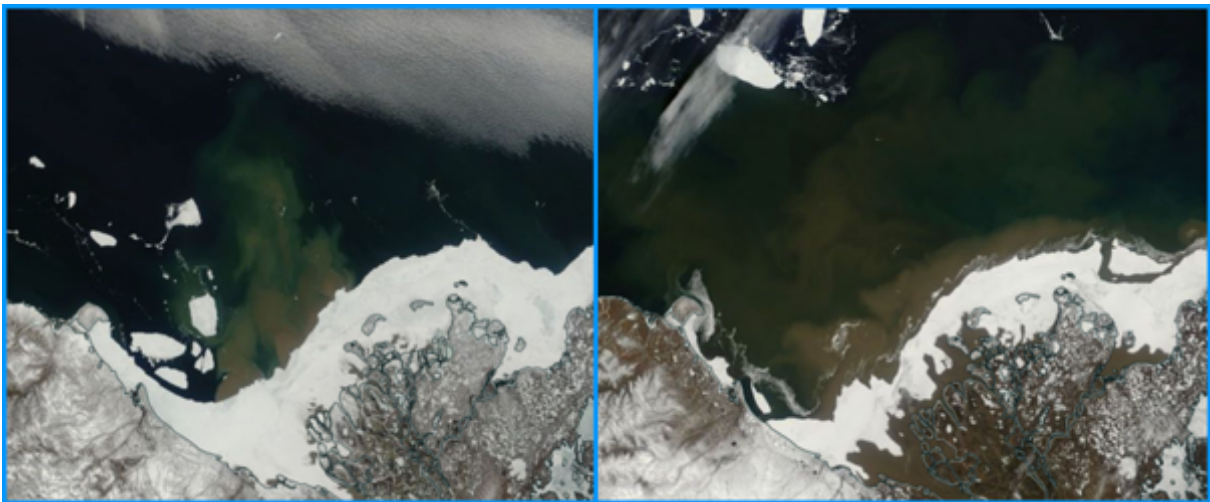
Fig 2.4: Satellite images of the partially ice-covered southern Mackenzie Shelf in 2016. The image on the left was taken on the 19th of May. The image on the right-hand side, featuring a tremendous sediment plume covering large parts of the Mackenzie Shelf, was taken on the 4th of June (image: worldview.earthdata.nasa.gov)

About 95 % of the total supplied sediment to the Mackenzie Shelf is contributed by the Mackenzie River, whereas a substantial amount of the sediment is supplied before ice break-up and most of the sediment during freshet in May and June (Hill et al., 1991). Fig. 2.4 shows satellite images of the sediment plume of the Mackenzie River in May and June 2016. Most of the hydrocarbons in the Mackenzie Delta are retrieved from the Devonian Canol formation

located in the lower Mackenzie River valley (Yunker et al., 2002). Deposits from the Canol formation contain immature bitumens, shales and coals.

Smaller rivers, like the Babbage River (Fig. 2.1), also contribute to the total supplied amount of sediment in the southern Beaufort Sea. Reported by Lewis and Forbes (1975) and Hill et al. (1991) (investigated in 1975 and 1976) the Babbage River supplies 0.35 Mt of sediment per year to the Mackenzie Shelf and Herschel Basin. Together with other smaller rivers of the surrounding area, like Firth and Malcolm River, the annual sediment supply to the Beaufort Shelf is estimated to be 1.45 Mt (Hill et al., 1991) and 0.02 Mt of POC (Macdonald et al., 1998). After Yunker et al. (2002), geochemical investigations exclude occurrence of petroleum-derived hydrocarbons in these smaller rivers.

Petroleum derived biomarkers are an additional potential source input to Herschel Basin. Wells like the Adlartok Well and the Immiugak Well, eastern of Herschel Island, as well as the Amauligak Well northeastern of the Mackenzie Shelf were investigated by Curiale (1991) and Snowdon et al. (2004). Oil spill of these wells can potentially alter the biomarker composition of sediments in Herschel Basin.

Additional terrigenous sediment can be supplied by coastal bluffs of the YCP. Major features of the Canadian Beaufort Sea coast are steep coastal cliffs, partially containing significant amounts of ground-ice, spits and barriers, as well as deltas of coastal plain rivers (Lewis and Forbes, 1975). The amount of sediment supplied by the YCP is 2.46 Mt per year (Hill et al., 1991) and 0.04 Mt of POC (Couture, 2010). The combined sediment load descending from these potential sources results in a sedimentation rate of 0.33 cm/a and a total deposition of 720,000 tons of sediment in Herschel Basin every year (Pfalz, 2017).

The pathway of terrigenous sediment issued mainly by the Mackenzie River can be influenced by a variety of factors. One of the factors with minor impact would be the tidal current in the southern Beaufort Sea. The range of the spring tide in this area amounts only 0.5 m (Huggett et al., 1975; Hill et al., 1991).

North-westerly and easterly winds have strong influence on the net sediment transport by directing of surface currents. The net sediment transport on the Beaufort Shelf is towards the east (Huggett et al., 1975; Hill et al., 1991). The report by Huggett et al. (1975) provides a broad background about the prevailing currents and the tidal situation on the Beaufort Shelf.

A potential influence on sedimentation in Herschel Basin is controlled by a coastal longshore current moving eastwards through "Workboat Passage" towards the Mackenzie Delta (Pelletier et al., 1984). This longshore current was discussed as an important pathway for SPM from Firth

and Malcolm River (Pelletier et al., 1984; Lantuit and Pollard, 2008), as well as for eroded deposits from the unglaciated YCP.

The Beaufort Gyre dominates clockwise movement of sea-ice and surface waters offshore but to a lesser extent influences circulation and sedimentation on the Beaufort Shelf (Carmack and Macdonald, 2002). The main coastal longshore currents of the study area are presented in Fig. 2.1 (Pelletier et al., 1984).

3.   Material & Methods

3.1.   Yukon Coast soil/sediment samples

All soil and sediment samples have been collected within the scope of the COPER project (**Co**astal **per**mafrost erosion, organic carbon and nutrient release in the Arctic nearshore zone). Aim of the project, which started in 2005, is to characterise sediment and OC transport in the Beaufort Sea, with a focus on the coastal erosion occurring on Herschel Island and the surrounding area. Character and velocity of the coastal erosion on Herschel Island is assessed by several methodical approaches (Fig. 3.1). Samples which were used in this thesis were taken during 2006, 2009, 2015 and 2016 YC (Yukon Coast) expeditions.
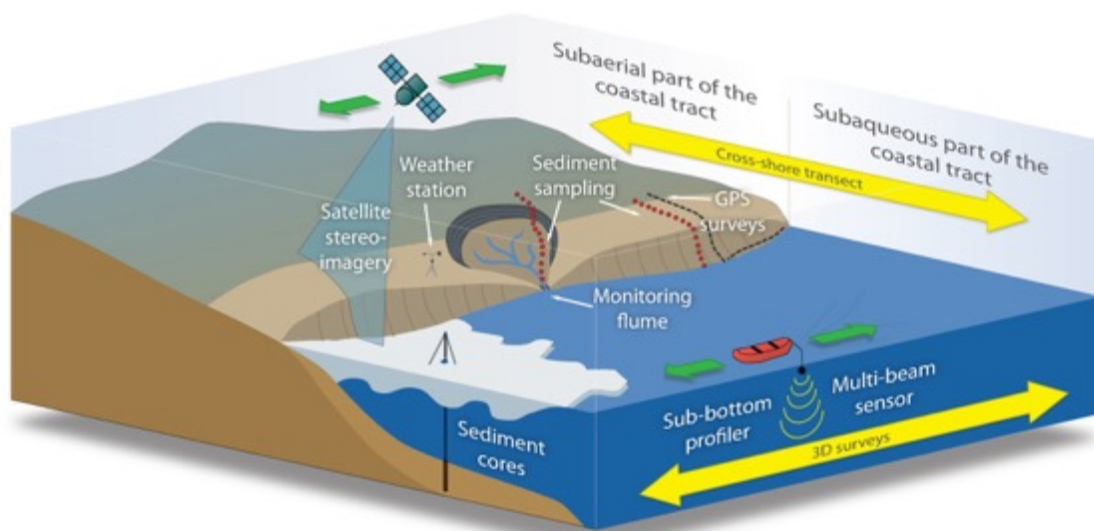
Fig. 3.1: Scheme of the methodical approach to assess the coastal permafrost erosion occurring on Herschel Island (image: AWI.de)

3.1.1. Herschel Island

3.1.1.1. Retrogressive thaw slump D

Soil samples collected on Herschel Island originate from two different outcrops (Table 3.1; Fig. 2.2). Five soil samples were taken from a large retrogressive thaw slump (RTS) at the southeastern coast of Herschel Island. Terminology of the so called "Thaw slump D" or "Slump D" varied from the 2009 to the 2015 expedition. Hence the differing sample ID "TSD" or "SlpD" depending on the time when the sample was taken. TSD, as this RTS is going to be called from now on, is the largest RTS on Herschel Island with a width of over 500 m (Lantuit et al., 2012b) and exposure of massive ground ice bodies (Fritz et al., 2011).

Two samples originating from TSD were sampled in 2006, whereas the other three were sampled in 2015. Fig. 3.2 shows the exact origin of the samples Slp15-PF-BIO01 until BIO03 in an outcrop of TSD. Additionally, the image shows glaciotectonic deformation which resulted from deformation by ice-thrusting of the LIS (Fritz et al., 2011).

Sample SlpD15-PF-BIO01 had a dark brownish colour with a substantial amount of plant residues and differed significantly from the samples SlpD15-PF-BIO02 and BIO03, which contained a sandy sediment fraction and, by optical judgment, distinctively lower TOC contents. All three samples showed a significant ice-rich composition. Both samples taken in the 2009 expedition showed very similar sediment properties as SlpD15-PF-BIO02 and BIO03.

Fig. 3.2: Glaciotectonic deformation in deposits of thaw slump D, showing origin of SlpD15-PF-BIO01 until BIO03 (image: G. Tanski/AWI)

3.1.1.2. Collinson Head/Retrogressive thaw slump B

The three samples labelled with the addition "Col" (Table 3.1) originate from a RTS located at Collinson Head (Fig. 2.2). Collinson Head marks the easternmost extent of Herschel Island. This study site will be referred to as TSB from now on. TSB is one of the smaller RTS on Herschel Island. Nevertheless, it also features up to 20 m thick ice bodies in its headwall and a width of about 150 m. TSB has firstly been reported after 1970, illustrating fast development of these erosional structures. Lantuit and Pollard (2005) reported an eroded sediment loss of 22300 m^3 between 1970 and 2004. High pore water salinities of samples from this deposit indicate a marine origin and hence support the theory of origin proposed by Bouchard (1974). All three samples from the TSB study site, derived from the 2009 YC expedition, had resembling sediment properties compared to the four described samples taken from the TSD study site.

Table 3.1: Summary of the soil samples from Herschel Island and the Komakuk Beach study site

study site	sample ID	TOC [%]	latitude	longitude
TSB	YC06-Col-2/1	1.5	69.571	138.867
	YC06-Col-2/26	0.6		
	YC06-Col-2/27	0.8		
TSD	TSD06-04-04	1.2	69.570	139.020
	TSD06-04-09	1.5		
	SlpD15-PF-BIO01	14.7		
	SlpD15-PF-BIO02	1.2		
	SlpD15-PF-BIO03	1.8		
Komakuk	YC09-PF-KOM-01-07	0.4	69.590	140.510
	YC09-PF-KOM-02-09	0.7		
	YC15-KOM-PF-BIO01	7.8	69.596	140.507
	YC15-KOM-PF-BIO02	1.8		
	YC15-KOM-PF-BIO03	0.9		
	YC15-KOM-PF-BIO04	0.4		
	YC15-KOM-PF-BIO05	12.6		

3.1.2.   Komakuk Beach/Yukon Coastal Plain

As reference of the unglaciated YCP westwards of Herschel Island, several soil samples from two study sites on Komakuk Beach were taken into account (Table 3.1). Komakuk Beach is located 60 kilometres to the west of Herschel Island (Fig. 2.1) close to the Alaskan border on the unglaciated part of the YCP (Fritz et al., 2012). The study site of the in 2015 collected soil samples featured an approximately 2.5 m high slope (Fig. 3.3). A profile of five samples was taken from this outcrop. Sample YC15-PF-BIO05 was taken from the top of the outcrop, out of the active layer. Sample YC15-PF-BIO01, taken directly below the active layer had an organic rich, peaty sediment distribution. Both samples contained high amounts of plant residues. YC09-PF-KOM-1-07 and YC09-PF-KOM-2-09 were sampled in the 2009 expedition and descend from the base of a second outcrop on Komakuk Beach. Both samples taken in the 2009 YC expedition showed a dark yellow, silty sediment distribution. The two samples exhibited high pore water salinities and might be of brackish or marine origin. All seven samples from the Komakuk Beach study site had a very ice-rich composition.

Fig. 3.3: Coastal outcrop located on Komakuk Beach featuring YC15-PF-KOM-BIO01 until BIO04 in consecutive order from top to bottom and the active layer sample YC15-PF-KOM-BIO05 (image: A. Irrgang/AWI)

3.1.3. Yukon Coast 2016 spring sediment samples

Table 3.2: <mark>All analysed sediment samples from Herschel Basin with the respective coordinates for study site</mark>

study site	sample ID	sediment depth [m]	water depth [m]	TOC [%]	latitude	longitude
<mark>Lc 1</mark>	PG 2303-1/2-1	0.94	38.3	1.0	69.51306	138.89503
	PG 2303-1/2-2	1.94		1.7		
	PG 2303-1/3-1	3.08		0.9		
	PG 2303-1/3-2	4.08		1.1		
	PG 2303-1/3-3	4.98		1.3		
	PG 2303-1/4-1	5.74		1.3		
	PG 2303-1/4-2	6.74		1.3		
	PG 2303-1/4-3	7.54		1.2		
	PG 2303-1/5-1	8.05		1.1		
	PG 2303-1/5-2	9.05		1.3		
	PG 2303-1/5-3	9.78		1.4		
	PG 2303-1/6-1	10.46		1.4		
	PG 2303-1/6-2	11.47		1.4		
	PG 2303-1/6-3	12.26		1.5		
	PG2303-7/0-1	surface		1.3		
	PG2303-7/1-2	0.01		1.0		
<mark>Lc 2</mark>	PG2302-1/0-1	surface	29.5	1.5	69.54604	138.92073
	PG2302-1/1-2	0.01		1.3		
<mark>Lc 3</mark>	PG2305-1/0-1	surface	9.2	1.1	69.56749	138.93628
	PG2305-1/1-2	0.01		1.1		
<mark>Lc 5</mark>	PG2307-1/0-1	surface	23.7	1.4	69.49263	138.95309
	PG2307-1/1-2	0.01		1.4		
<mark>Sc 7</mark>	PG2308-1/0-1	surface	36.7	1.1	69.54073	138.91689
	PG2308-1/1-2	0.01		1.0		
<mark>Sc 11</mark>	PG2312-1/0-1	surface	15.0	0.4	69.55621	138.92415
	PG2312-1/1-2	0.01		1.0		
<mark>Sc 12</mark>	PG2313-1/0-1	surface	~ 5	2.1	69.57433	138.93907
	PG2313-1/1-2	0.01		1.2		
<mark>Sc 13</mark>	PG2315-1/0-1	surface	50.3	1.5	69.50405	138.91635
	PG2315-1/1-2	0.01		0.9		
<mark>Sc 14</mark>	PG2316-1/0-1	surface	43.0	1.4	69.49689	138.93561
	PG2316-1/1-2	0.01		1.0		
<mark>Sc 19</mark>	PG2318-1/0-1	surface	15.0	1.3	69.4914	138.95892
	PG2318-1/1-2	0.01		1.0		

All analysed sediment samples have been obtained during the Yukon Coast 2016 spring (YC16 spring) expedition conducted by the COPER team of the AWI. The expedition was scheduled from the mid of April to the mid of May. Aim of the expedition was to track the pathway of coastally eroded deposits and OC from Herschel Island in the nearshore area and, furthermore, to confine the regional sea-level history and to obtain a high-resolution Holocene climate record.

Gravity cores have been taken along two cross-cutting transects in Herschel Basin (Fig. 2.2). Transect A progresses from Pauline Cove (Fig. 2.2) towards the centre of Herschel Basin. Transect B is located parallel to the coast of Herschel Island progressing from the YCP towards the sample location of Lc 1 (Fig. 2.2). Gravity cores have been taken to obtain the undisturbed sediment surface, using a gravity corer (UWITEC corp.) with 60 cm PVC liners (6 cm diameter). In total 17 short cores have been taken from throughout both transects. For obtaining longer sediment cores we used a piston corer (UWITEC corp.) operated via a tripod (Wagner, 2003). During the coring process, the tripod (Fig. 3.4) was mounted on the approximately 1.60 m thick sea ice.
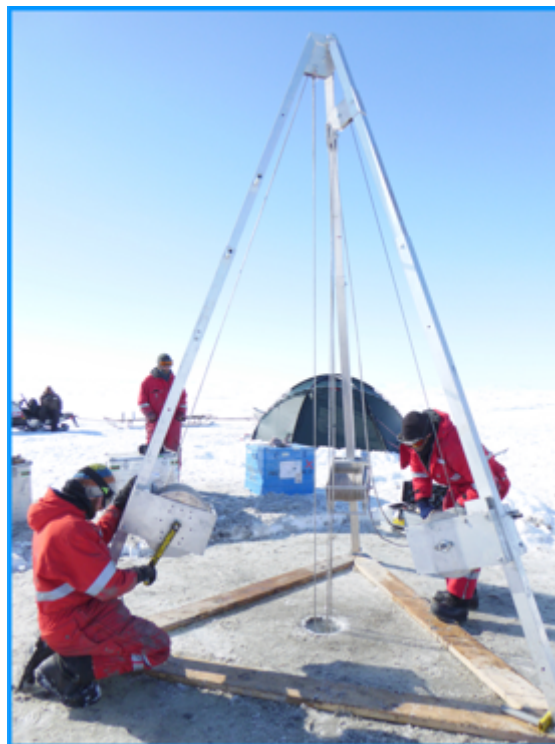
Fig. 3.4: The sediment core PG 2303 is retrieved from the the Lc 1 sample location (image: B. Biskaborn/AWI)

3.1.3.1. Surface sediment samples, Herschel Basin

From the 17 gravity cores taken in April to May 2016, ten have been used in this thesis (Table 3.2; Fig. 2.2). Samples were retrieved from the first and the second centimetre of the ten gravity cores. All surface sediment samples are about equally distributed over transect A and B, to obtain a widespread overview over the geochemistry of Herschel Basin (Fig. 2.2). Sediment properties of the gravity core samples were similar as of the PG 2303 core (see paragraph 3.1.3.2.). Gravity cores located closer to the shore of Herschel Island contained fine sandy sediment layers at irregular intervals. Some surface sediment samples occasionally contained ice-rafted pebbles.

3.1.3.2. Sediment core PG 2303, Herschel Basin

The sediment core PG 2303 was taken at the transection of transect A and transect B at a water depth of 38.3 m (69°30´47.0´´N; 138°53´42.1´´W). PG 2303-1/2-6 (**P**eri**g**lacial 2303-1/2-6; study site Lc 1), from now on just referred to as PG 2303, has a total length of 12.29 m. 14 samples throughout PG 2303 were analysed in this thesis (Table 3.2). The age-depth model (Fig. 3.5) was taken from the master thesis of Gregor Pfalz (2017). Radiocarbon results of this age model were analysed on several specimens of *Nuculana sp.*. The sedimentation rate of PG 2303 shows an almost linear progression throughout the entire sediment core (0.33 cm/a). The sediment core bottom at 12.29 mbsf has a deposition age of about 4.35 ka BP.
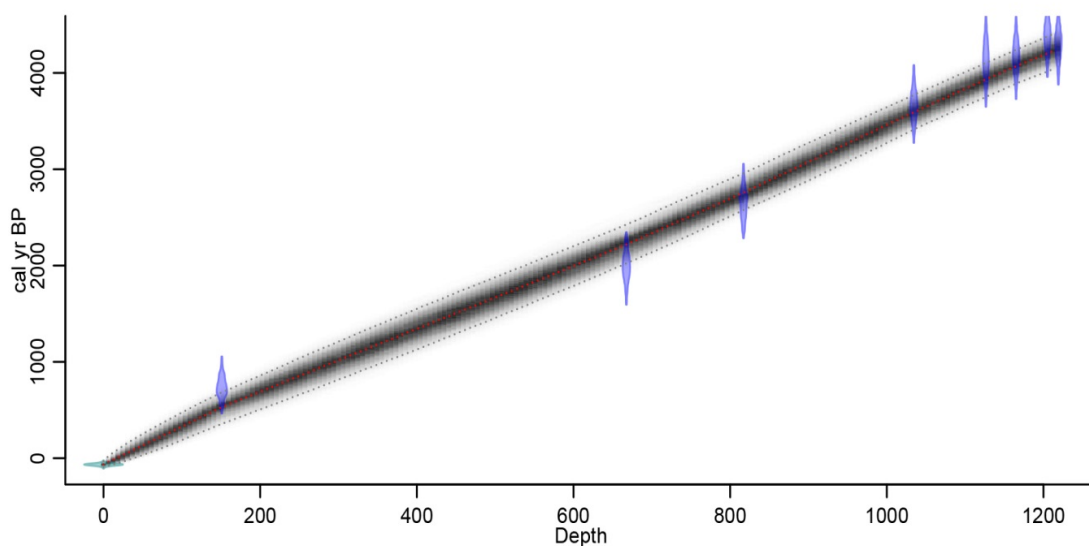
Fig. 3.5: Age-depth model of PG 2303 by Pfalz (2017). The depth is indicated in cm

Colour and grainsize of PG 2303 featured almost no change throughout the entire core. PG 2303 had a brown-greyish to greyish-black colour. From time to time the sediment core exhibited fine fissures and cavities of gas inclusion (Pfalz, 2017). Smears of black organic-rich material, which emitted a slight sulfidic smell, were distributed over some parts of PG 2303. The whole core showed no evidence for stratification. Grain size analyses conducted by Pfalz (2017) revealed marginal variation throughout the entire core. Grain size of PG 2303 can be described as "silt" or "clayey silt".

3.2. Preparation of biomarker samples

3.2.1. Sample extraction

All sample preparations and biomarker analyses were conducted in the organic geochemistry laboratories at the AWI in Bremerhaven.

All 49 soil and sediment samples were extracted and processed according to established standard procedures of the organic geochemistry group at the AWI (Meyer et al., 2016). All samples were ultrasonically extracted three times for ten minutes each, using 25 ml of a 9:1 (vol/vol) dichloromethane (DCM) and methanol (MeOH) solvent mixture for every run. After each run the samples were centrifuged and the supernatant decanted. Each total lipid extract (TLE) was concentrated by evaporation with a rotary evaporator and transferred into 4 ml glass vials.

To reconstruct potential error propagation, a laboratory internal sediment standard was used additionally with every sediment extraction and analysed in every sequence.

3.2.2. Saponification

All samples were saponified (modified after Sakata et al. (2008)), using approximately 1.5 ml of a 0.1 M potassium hydroxide (KOH; 5.67 g/l) solution diluted in MeOH and H_2O (9:1; vol/vol). Samples were saponified to isolate fatty acids from the lipid extract. The fatty acid containing fraction was not used in this thesis. After the saponification, TLE's were heated for two hours at 80 °C. Neutral lipids (e.g., hydrocarbons and alcohols) were extracted from the saponified solution through liquid-liquid-extraction. Hydrocarbons and alcohols were separated by adding *n*-hexane. Each liquid-liquid-extraction was repeated three to four times.

3.2.3.   Silica gel column chromatography

Individual biomarker compound classes of each neutral-lipid fraction were isolated by applying a simple column chromatography modified after Eglinton and Hamilton (1967). Different fractions were separated through a self-built silica gel column (4 cm of dry silica gel, pre-combusted at 450 °C). The first fraction, containing the saturated *n*-alkanes and hopanoid compounds, was eluted with *n*-hexane. The second and third fraction, which contained PAH's (polycyclic aromatic hydrocarbon; eluted with *n*-hexane and DCM; 9:1; vol/vol) and ketones (eluted with *n*-hexane and DCM; 2:1; vol/vol), were not used in this thesis. A fourth fraction containing polar components, such as the required GDGT's, was eluted with MeOH. Each fraction was eluted with 3.5 ml of the respective solvent mixture. After isolation, both fractions were concentrated by evaporation under a steady stream of dry N_2.

The original intention of analysing PAH biomarkers was impeded, as preliminary analyses revealed a contamination of the surface sediment samples. Tests showed that the contamination was most likely caused through sample storage and transport in Whirl-Pak bags.

3.2.4.   Processing of GDGT fractions

Prior to the analyses of the GDGT's, polar fractions were filtered over 0.45 μm pore size hydrophilic PTFE syringe filters, using a solvent mixture of *n*-hexane and isopropanol (99:1; vol/vol). The filtration was repeated three times using about 100 μl of the solvent mixture for each filtration process. Purpose of this measure was to remove remaining particles which are a potential threat to the HPLC.

The filtered polar fractions were eventually weighed to determine GDGT concentrations for each sample. According to the weight, every sample was individually diluted for analyses on the HPLC.

3.3.   Biomarker analysis

3.3.1.   GC-MS analysis

Hopanoid compounds were analysed on an Agilent 6850 gas chromatograph (GC) -system (with Agilent J&W DB-1MS column; length 30 m; diameter 250 μm) connected to an Agilent 5975C VL MSD quadrupole mass spectrometer using helium as carrier gas.

Hopanoid fractions were analysed in selected ion monitoring (SIM) mode for increased sensitivity and diluted with *n*-hexane. The initial temperature of the oven was set to 60 °C for three minutes. Subsequently the oven was heated to 150 °C with a rate of 20 °C per minute and to 320 °C at a rate of four °C per minute. This temperature was maintained for 15 minutes. Hopanoids were identified by comparing selected ion chromatograms with the key fragment of the ion at *m/z* = 191, with published data of Wenger and Isaksen (2002) (Fig. 3.6). Quantification of hopanoid biomarkers was achieved by using a single point calibration. An external standard containing 2.71 ng/μl (diluted in *n*-hexane) of a $C_{30}17\beta(H), 21\beta(H)$-Hopane was repeatedly analysed with every sequence. Calculated concentrations should be considered as semi-quantitative. Quantified results of hopanes, *n*-alkanes and fractional abundances of the GDGT's are listed on the Open Access library PANGAEA.

The error between analysed $C_{30}17\beta(H), 21\beta(H)$-Hopane peak areas was determined with two independent series of sequences. For the first series of the analysed hopane standard, including eight samples, peak areas deviated by 31.8 %. The second error of 24.1 % was determined with ten analysed hopane standards. Both values result in a mean of 28.0 %.
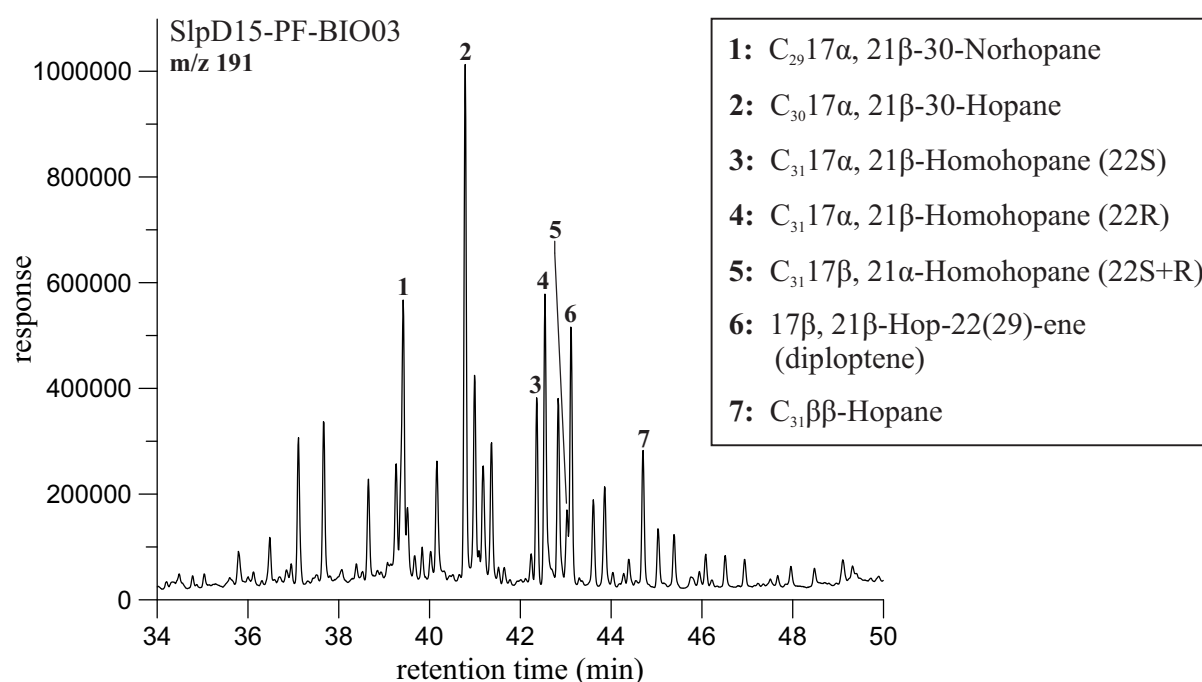
Fig. 3.6: Chromatogram showing hopanoid compounds of SlpD15-PF-BIO03 (*m/z* 191). Hopanoid compounds were identified after Wenger and Isaksen (2002)

The relative state of degradation of the hopanoid composition in a sample can be assessed with the Hopanoid-Index (Ep. 1). With depletion of the thermally labile $C_{31}\beta\beta$ Hopane and relative enrichment of the $C_{31}17\alpha$, 21β-Homohopane (22S) and $C_{31}17\alpha$, 21β-Homohopane (22R) and subsequently $C_{31}17\beta$, 21α-Moretane, the degradation of each sample can be assessed (compare paragraph 1.3.1. concerning diagenesis of bacteriohopanetetrol (Peters et al., 2005)).

$$\text{Hopanoid} - \text{Index} = \frac{C_{31}\beta\beta}{C_{31}\beta\beta + C_{31}\alpha\beta S + C_{31}\alpha\beta R + C_{31}\beta\alpha S + R} \tag{1}$$

3.3.2. GC-FID analysis

n-alkane (normal alkanes) biomarkers were analysed via gas chromatography coupled to a flame ionization detector (FID). Helium was used as carrier gas. The used device was an Agilent 7890A GC system, equipped with an Agilent J&W DB-5ms column (length 60 m; diameter 250 μm). *n*-alkane containing fractions were injected with *n*-hexane. $C_{14} - C_{36}$ *n*-alkanes, pristane and phytane, were identified and quantified. For identification of the *n*-alkane homologue series the retention time of the compounds were compared to an external alkane standard ($C_{10} - C_{40}$, odd and even *n*-alkanes plus pristane and phytane, 2 ng/μl). The alkane standard was included twice with every sequence.

n-alkanes were quantified against the external alkane standard. $C_{14} - C_{36}$ *n*-alkanes plus pristane and phytane of the external *n*-alkane standards were quantified and averaged for each sequence. Identified *n*-alkane compounds were quantified with a single point calibration of the external *n*-alkane standard. The averaged error of all quantified standard compounds is 7.83 %. This value was calculated via the standard deviation (SD) of averaged *n*-alkane standard peak areas from four individual sequences.

The distribution of odd over even numbered alkanes, represented by the carbon preference index (CPI; Cooper and Bray, 1963; Marzi et al., 1993; Simoneit, 1977), can be used as a source indication for lipid composition. The CPI, stated in Eq. 2, was modified after Jeng (2006). CPI values > 1 indicate a terrestrial n-alkanes source (Eglinton and Hamilton, 1967). Whereas more balanced ratios between odd and even numbered n-alkanes can indicate thermal maturity and petrogenic origin of the lipid composition (Bray and Evans, 1961; Simoneit, 1984).

$$\text{CPI} = \frac{1}{2}\left(\frac{n\text{C}_{23} + n\text{C}_{25} + n\text{C}_{27} + n\text{C}_{29} + n\text{C}_{31}}{n\text{C}_{22} + n\text{C}_{24} + n\text{C}_{26} + n\text{C}_{28} + n\text{C}_{30}} + \frac{n\text{C}_{23} + n\text{C}_{25} + n\text{C}_{27} + n\text{C}_{29} + n\text{C}_{31}}{n\text{C}_{24} + n\text{C}_{26} + n\text{C}_{28} + n\text{C}_{30} + n\text{C}_{32}}\right) \quad (2)$$

The terrestrial aquatic ratio (TAR; ep. 3) (Bourbonniere and Meyers, 1996) assesses the relative contribution of terrestrial and aquatic distribution of n-alkanes. With increasing ratio of long-chain n-alkanes from epicuticular waxes (C_{27}, C_{29} and C_{31} n-alkanes) over short-chain n-alkanes produced by algal communities (C_{15}, C_{17} and C_{19} n-alkanes) the TAR ratio increases.

$$\text{TAR} = \frac{n\text{C}_{27} + n\text{C}_{29} + n\text{C}_{31}}{n\text{C}_{15} + n\text{C}_{17} + n\text{C}_{19}} \quad (3)$$

Sphagnum-derived OM from peat deposits can be assessed via various n-alkane *Sphagnum* proxies.

Due to the characteristic occurrence of C_{23} and also C_{25} n-alkanes, *Sphagnum* contribution in terrestrial OM can be assessed with the $C_{23}/(C_{23} + C_{29})$ n-alkane ratio (Nichols et al., 2006; van Dongen et al., 2008) and the $C_{25}/(C_{25} + C_{29})$ n-alkane ratio (Vonk et al., 2015).

n-alkane distributions will be used to distinguish between different sources that supply Herschel Basin with sediment. Findings within n-alkane distributions will be compared with other indices to reinforce results.

Standard deviations for all stated CPI, TAR and C_{23}:C_{29} ratios were determined by analysis of the laboratory internal sediment standards. The calculated standard deviation for the CPI is 0.06 (1.28 %). Results of the TAR had a standard deviation of 4.63 (17.43 %), whereas the ratio of the C_{23} n-alkane versus the C_{29} n-alkane showed a standard deviation of 0.015 (6.48 %).

3.3.3. HPLC analysis

GDGT's were analysed by high-performance liquid chromatography (HPLC) coupled with an atmospheric pressure chemical ionization (APCI) interface connected to a single quadrupole mass spectrometer (MS). The used devices were an Agilent 1200 series HPLC system and an Agilent 6120 single quadrupole MS. For separating individual GDGT compounds, a Prevail Cyano column (Grace, 3 μm, 150 mm x 2.1 mm), maintained at 30 °C, was used. The used method was modified after Hopmans et al. (2000). Depending on the weight of the polar fraction, sample injection varied between 5, 10 or 20 μl (99:1; n-hexane:isopropanol; vol:vol). After sample injection and five minutes isocratic elution with the mobile phase A (n-hexane/isopropanol/chloroform; 98:1:1; vol:vol) at a flow rate of 0.2 ml/min, the proportion of the mobile phase B (n-hexane/isopropanol/chloroform; 89:10:1; vol:vol) was linearly increased up to 10 % within 20 minutes. Subsequently, mobile phase B was linearly increased to 100 % within ten minutes. This state was kept for seven minutes, before cleaning the column in backflush mode for five minutes at a flow rate of 0.6 ml/min. Before analysis of the following sample, the column was re-equilibrated with mobile phase A at a flow rate of 0.2 ml/min for ten minutes.

GDGT compounds were detected via positive-ion APCI-MS and SIM of the $(M+H)^+$ ions (Schouten et al., 2007a). The APCI spray-chamber conditions were set as described hereafter. The nebulizer pressure was set to 50 psi at a vaporizer temperature of 350 °C. The flow of N_2 drying gas was 5 l/min at 350 °C. Capillary voltage was set to -4 kV and corona current to +5 μA.

For TEX/BIT analyses, the MS-detector was set to SIM for the following $(M+H)^+$ ions: m/z 1302.3 (GDGT 0), 1300.3 (GDGT 1), 1298.3 (GDGT 2), 1296.3 (GDGT 3), 1292.3 (GDGT 4 + 4′ / crenarchaeol + regio-isomer), 1050 (GDGT III), 1036 (GDGT II), 1022 (GDGT I) and 744 (C_{46} standard), with a dwell time of 67 ms per ion.

The GDGT distribution of each sample is stated as fractional abundance. Fractional abundances were calculated with the respective peak areas of each GDGT.

The branched and isoprenoid tetraether (BIT) index can be used to assess the fate of soil organic carbon in aquatic environments (Hopmans et al., 2004). The BIT index quantifies the relative abundance of branched GDGT's (Sinninghe Damsté et al., 2000) and crenarchaeol (Sinninghe Damsté et al., 2002). Crenarchaeol is always found in marine settings, but can occur in lacustrine environments as well (Powers et al., 2004; Schouten et al., 2000) and has furthermore

been detected in peat deposits (Weijers et al., 2004; Weijers et al., 2006b). Nevertheless, concentrations of crenarchaeol in soils remain at a comparable low constant level (Ochsenreiter et al., 2003), hence large interference on BIT values are not to be expected. Branched GDGT's are mostly synthesised by anaerobic bacteria living in soil and peat (Weijers et al., 2006a; Weijers et al., 2009) and can therefore be used to trace terrestrial produced OM in aquatic systems.

$$\text{BIT index} = \frac{[\text{I}] + [\text{II}] + [\text{III}]}{[\text{I}] + [\text{II}] + [\text{III}] + [\text{GDGT 4}]} \tag{4}$$

The roman numbers in equation 4 refer to the three branched GDGTs, GDGT I (m/z 1022), GDGT II (m/z 1036) and GDGT III (m/z 1050). GDGT 4 refers to crenarchaeol without the associated regio-isomer. BIT values can vary between 0 and 1. A BIT values of 1 equals 100 % abundance of branched GDGT compounds.

The standard deviation of the BIT index was also determined via the laboratory internal sediment standard. The resulting standard deviation of seven analysed sediment standards for the BIT index was 0.04 (5.29 %).

3.4.   Preparation and analysis of radiocarbon samples

Each bulk organic radiocarbon sample was prepared and analysed in the laboratories of the AWI in Bremerhaven. Radiocarbon dating was conducted to assess the influence of various potential sediment suppliers on the bulk radiocarbon composition of sediments in Herschel Basin.

In total 46 soil and sediment samples were prepared for accelerator mass spectrometry (AMS). Each sample was weighed into a silver capsule to equally obtain about 1 mg of carbon, according to the samples associated TOC value. This guideline was strictly adhered to remain within the measurability of the used AGE 3 system (see paragraph 3.4.2.).

Samples PG 2303-1/5-1, 6-1 and 6-2 were not radiocarbon dated, as they failed to graphitise on the AGE 3 system.

3.4.1.   Acidification

For removal of inorganic carbon and to reduce contamination effects (Kirner et al., 1995), samples designated for AMS analysis were treated after an acidification protocol. Beforehand the actual acidification, all samples were wetted with 2 drops of ethanol. Subsequently, after heating the samples up to 60 °C, the samples were treated with 6 N hydrochloric acid (HCl) in three steps (Step 1: 4 drops; step 2: 3 drops; step 3: 2 drops of 6 N HCl). In between each step the protocol prescribed 20 minutes of latency. The treated samples were dried overnight at 60 °C to assure there were no residues of HCl remaining.

3.4.2.   Graphitisation

All samples were analysed on an AGE 3 system (Automated Graphitization System) by Ionplus (Wacker et al., 2010b). The AGE 3 combines sample combustion, an elemental analyser (EA) and graphitisation in one fully automated system.

Prior to the graphitisation process, decarbonated samples were packed into tin capsules. Samples were combusted with helium as carrier gas. The resulting gasses were chromatographically separated and CO_2 collected in a zeolite trap. After creating a pressure gradient by heating the zeolite trap to 450 °C, the CO_2 is released into a reactor to start the graphitisation. Post reaction and pressure stabilisation, the sample is immediately pressed into graphite targets to prevent interaction with air (Wacker et al., 2010b).

3.4.3.   Accelerator mass spectrometry

Graphite targets were analysed on a Mini Carbon Dating System (MICADAS; Ionplus) (Synal et al., 2007). The MICADAS system is the smallest AMS spectrometer of its kind.

The obtained error of all analysed bulk soil and sediment samples is attached in Table 4.1. The uncertainty was determined from the counting statistic of analysed samples and blanks (Wacker et al., 2010a). Variance of blank analyses determined sample contamination and contamination through the ion source of the MICADAS system. A standard error of 0.5 % was assigned to each ^{14}C result.

Results of AMS analyses include radiocarbon ages and fraction modern values ($F^{14}C$). $F^{14}C$ expresses the deviation of the $^{14}C/^{12}C$ ratio of the sample, with an applied correction for fractionation, to the $^{14}C/^{12}C$ ratio of a modern carbon standard (Stuiver and Polach, 1977; Reimer et al., 2004).

$$t = -8033 \times \ln(F^{14}C) \tag{5}$$

$F^{14}C$ values of radiocarbon values taken from the literature were calculated after Stuiver and Polach (1977) (Eq. 5), with t as the ^{14}C age of the respective sample and the Libby half-life of 5568 years for consistency (mean life 8033 years). In Stuiver and Polach (1977), $F^{14}C$ is referred to as A_{SN}/A_{ON}.

4.   Results

4.1.   TOC values

Previously obtained TOC values, analysed on different devices at AWI Potsdam and AWI Bremerhaven, could not be reproduced during the graphitisation process. During the graphitisation process, unusually low CO_2 concentrations were detected indicating inaccuracy of previously analysed TOC values of some samples. All TOC values were therefore coherently determined with the, to the AGE 3 system coupled EA (Table 3.1 and 3.2). The precision of the TOC measurements was determined by quantification of the oxalic acid (Ox-2) standard (Stuiver and Polach, 1977; Wacker et al., 2010b). The error of analysed Ox-2 standards, calculated with the associated standard deviation, is 1.6 %. Calculations for sample PG 2303-1/6-3 resulted in a standard deviation of 0.1 for an averaged TOC content of 1.5 %. This value was determined with three incoherent analyses of PG 2303-1/6-3.

4.2.   Hopane triterpenes

The most abundant hopanoid compounds in the surface sediment samples from Herschel Basin are diploptene, $C_{29}\alpha\beta$ and $C_{30}\alpha\beta$ (Fig. 5.1). Other abundant hopanoid compounds are $C_{31}\alpha\beta S$ and $C_{31}\alpha\beta R$ as well as $C_{31}\beta\beta$ hopanes. Values calculated with the Hopanoid-Index (Eq. 1) of all analysed samples range between 0.21 and 0.52. The individual result of each sample is illustrated in Fig. 4.1. The average Hopanoid-

Index of samples from Herschel Island is 0.35 (SD = 0.07), not including SlpD15-PF-BIO01 (Hopanoid-Index = 0.52) as this samples value deviates distinctively from the stated average composition. The average value of samples combined for all samples from both Komakuk Beach study sites is 0.38 (SD = 0.08; except YC15-KOM-PF-BIO02).

Analysed surface sediment samples show an average value of 0.45 (SD = 0.03), similar as the average results of PG 2303 samples (0.46 (SD = 0.04); Fig. 5.7).

The relative composition of $C_{29}17\alpha$, 21β-30-Norhopane, $C_{30}17\alpha$, 21β-Hopane and diploptene (17β, 21β-Hop-22(29)-ene) of all soil and sediment samples is presented in Fig. 5.1. Soil samples retrieved from outcrops on Herschel Island show high abundance of the diagenetic hopanes $C_{29}\alpha\beta$ and $C_{30}\alpha\beta$, apart from sample SlpD15-PF-BIO01. This particular sample has a different hopanoid distribution with diploptene as the most abundant hopanoid compound (Fig. 5.1).

The hopanoid distribution of samples retrieved from the Komakuk Beach study sites show strong variation within Fig. 5.1. YC09-PF-KOM-01-07 and YC09-PF-KOM-02-09 feature a similar distribution compared to samples retrieved from Herschel Island, whereas YC15-PF-KOM-BIO01, YC15-PF-KOM-BIO03 and YC15-PF-KOM-BIO05 feature high abundance of diploptene, similar as SlpD15-PF-BIO01.

Hopanoid biomarkers of sediment samples shown in Fig. 5.1 indicate an intermediate composition of the three hopanoid compounds. Diploptene concentrations of the surface samples range between 3.49 and 14.50 ng/g TOC. The results are shown in Fig. 4.3.
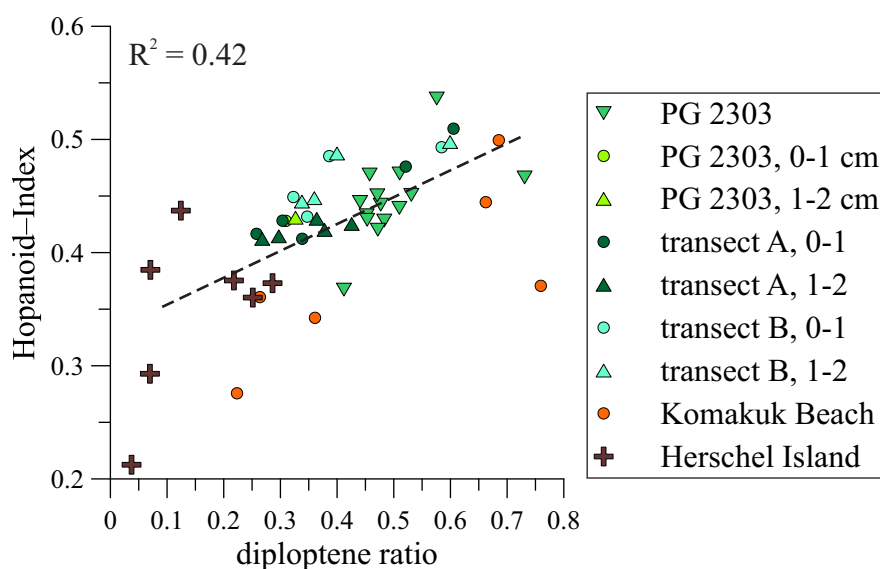
Fig. 4.1: Correlation of the Hopanoid-Index and the diploptene ratio (diploptene/(diploptene + $C_{29}\alpha\beta + C_{30}\alpha\beta$)). Surface sediment samples are differently colored and assigned according to their location in Herschel Basin

4.3. *n*-alkanes

CPI results of all samples retrieved from Herschel Island have a mean value of 4.3 with a standard deviation of 2.7. TAR calculations of the same eight samples show a wide range of results from 1.7 to 53.5. The TAR value of 53.5 was calculated with *n*-alkane compounds of SlpD15-PF-BIO01. CPI results of the remaining seven samples from Herschel Island have a standard deviation of 1.9. Calculations of the C_{23}:C_{29} ratio of all eight samples from Herschel Island produced a mean value of 0.30 with standard deviation of 0.09 (Fig. 4.2).

Samples from the Komakuk Beach study site show a CPI mean of 9.3 (SD = 3.7). The TAR mean of samples from Komakuk Beach is 22.4 (SD = 9.8). The ratio of the C_{23} *n*-alkane to the C_{29} *n*-alkane show a mean value of 0.25 (SD = 0.12; Fig. 4.2). *n*-alkane results of samples from Komakuk Beach display strong variation in all calculated values.

CPI values of the surface sediment samples are presented in Fig. 4.3. All values show closely resembling values with a mean of 4.5 (SD = 0.6). C_{23}:C_{29} ratios display a very low variance with a mean of 0.29 (SD = 0.01). The mean result of the TAR of all surface sediment samples is 7.4 (SD = 2.1; Fig. 4.2).

The downcore variation of CPI and the C_{23}:C_{29} ratio in PG 2303 is illustrated in Fig. 5.7. *n*-alkane results of PG 2303 are also presented in Fig. 4.2. CPI results of PG 2303 show a mean of 4.4 (SD = 0.5). The mean value of the TAR, calculated with the 14 PG 2303 samples, is 3.2 (SD = 3.2). C_{23}:C_{29} ratios show a similar mean as the surface sediment samples from Herschel Basin (mean = 0.31; SD = 0.02).

Fig. 5.3 comprises four saturate fraction chromatograms of the samples PG 2302-1/1-2 (Lc 2 study site), PG 2303-7/1-2 (Lc 1), PG 2303-1/2-2 (Lc 1), SlpD15-PF-BIO01. These four chromatograms, linked to the respective position in Fig. 5.3, display UCM's of varying development. The chromatograms are showing the homologue series of the *n*-alkanes.

Fig. 4.2: A: $C_{23}:C_{29}$ ratio plotted against the TAR, showing a coherence in all analysed samples and samples from Yunker et al. (1992). Literature data comprises Mackenzie River SPM (red and purple diamonds) and soil samples from the glaciated YCP (brown rectangles); B: $C_{23}:C_{29}$ results plotted against results of the BIT index; C: Correlation between TAR and CPI values; D: $C_{23}:C_{29}$ ratios plotted against the CPI indicate a similar distribution as shown in plot A

4.4. GDGT's

Soil samples from Herschel Island show a mean BIT value of 0.88 (SD = 0.17; Fig. 4.2). Calculated BIT values of the samples YC06-Col-2/26 and YC06-Col-2/27 from the TSB study site display relatively low values of 0.51 and 0.75 respectively.
The five soil samples from the outcrop on Komakuk Beach (Fig. 3.3) feature highest BIT values with a mean of 0.97 (SD = 0.07). Both samples taken in the 2009 YC expedition show lower BIT values of 0.75 (YC09-KOM-PF-2-07) and 0.61 (YC09-KOM-PF-2-09).
BIT calculations of the surface sediment samples from Herschel Basin resulted in a mean of 0.78 (SD = 0.04). Fig. 4.4 shows BIT values of the surface sediment samples distributed over Herschel Basin.
BIT values of the sediment core PG 2303 show a mean of 0.76 (SD = 0.03; Fig. 4.2). The downcore evolution of BIT values analysed on the 14 samples of PG 2303 is presented in Fig. 5.7.

4.5. Geochronology

Table 4.1: Radiocarbon results of all analysed soil and sediment samples (continued on page 34). Soil $\delta^{13}C$ data was obtained from Dr. Michael Fritz/AWI

study site	sample ID	^{14}C age [ka BP]	^{14}C error [± yr BP]	$F^{14}C$	$F^{14}C$ error [%]	$\delta^{13}C$ [‰]
TSB	YC06-Col-2/1	32.89	459	0.02	5.72	-26.30
	YC06-Col-2/26	26.95	259	0.04	3.22	-26.30
	YC06-Col-2/27	27.60	271	0.03	3.37	-25.80
TSD	TSD06-04-04	30.99	394	0.02	1.58	-26.40
	TSD06-04-09	19.28	127	0.09	4.90	-26.50
	SlpD15-PF-BIO01	9.76	72	0.30	0.90	-26.98
	SlpD15-PF-BIO02	22.30	77	0.06	0.96	-26.17
	SlpD15-PF-BIO03	16.55	113	0.13	1.40	-26.54
Komakuk	YC09-PF-KOM-01-07	20.72	155	0.08	1.93	-25.12
	YC09-PF-KOM-02-09	18.18	128	0.10	1.59	-25.70
	YC15-KOM-PF-BIO01	8.30	67	0.36	0.84	-27.69
	YC15-KOM-PF-BIO02	8.38	81	0.35	1.01	-27.65
	YC15-KOM-PF-BIO03	10.69	123	0.26	1.53	-27.73
	YC15-KOM-PF-BIO04	16.26	238	0.13	2.96	-28.42
	YC15-KOM-PF-BIO05	8.00	67	0.37	0.83	-27.92

Results of AMS radiocarbon dating are given in Table 4.1. The δ^{13}C data was received from the master thesis of Pfalz (2017) and from Dr. Michael Fritz (AWI Potsdam).

Soil samples from Herschel Island show strong variations in radiocarbon org. ages with a mean value of 23.29 ka BP (SD = 7.83 ka BP). Especially SlpD15-PF-BIO01 is noticeable with a radiocarbon age of 9.76 ka BP. F^{14}C results of all soil samples from Herschel Island, except SlpD15-PF-BIO01 (F^{14}C = 0.30), show a mean of 0.06 (SD = 0.04). δ^{13}C values of all eight samples from Herschel Island have a mean value of -26.37 ‰ (SD = 0.34 ‰).

Radiocarbon ages from the soil profile on the Komakuk study site show increasing values from top to bottom. The obtained ages for the five soil samples range from 8.00 to 16.26 ka BP from top to bottom. The two additional samples descending from the Komakuk Beach study site, taken from the base of a second outcrop, exhibit radiocarbon ages of 18.18 and 20.72 ka BP. Associated F^{14}C results of all seven samples from Komakuk Beach range from 0.08 to 0.37. The δ^{13}C results display a mean of -27.18 ‰ (SD = 1.25 ‰).

Radiocarbon results of the first centimetre of all surface sediment samples feature a mean of 11.78 ka BP (SD = 1.67 ka BP). The mean value of the second centimetre of the surface sediment samples is 11.95 ka BP (SD = 1.99 ka BP). Data of samples from both transects show a slight overall trend of increasing values towards the basin centre. This trend can be observed in both, the first and the second centimetre of the gravity cores (Fig. 4.4). Associated mean F^{14}C values of the first centimetre of the surface samples are 0.25 (SD = 0.07) and 0.22 (SD = 0.04) for the second centimetre of all surface samples. All surface sediment samples show very close resembling δ^{13}C results with a mean of -26.13 ‰ (SD = 0.25 ‰).

Bulk organic ^{14}C results of PG 2303 display an overall increase from top to bottom and an overall decrease in F^{14}C results. The values range from 6.71 ka BP to 16.10 ka BP (Table 4.1). F^{14}C values vary from 0.43 to 0.13. The δ^{13}C mean of associated sediment samples is -25.95 ‰ (SD = 0.10 ‰).

Table 4.1: continued

study site	sample ID	¹⁴C age [ka BP]	¹⁴C error [± yr BP]	F¹⁴C	F¹⁴C error [%]	δ¹³C [‰]
Lc 1	PG 2303-1/2-1	10.78	56	0.26	0.70	-25.83
	PG 2303-1/2-2	6.71	64	0.43	0.80	-26.00
	PG 2303-1/3-1	11.58	59	0.24	0.73	-25.93
	PG 2303-1/3-2	12.81	61	0.20	0.76	-26.11
	PG 2303-1/3-3	13.95	92	0.18	1.15	-25.88
	PG 2303-1/4-1	13.45	62	0.19	0.77	-25.99
	PG 2303-1/4-2	14.23	64	0.17	0.80	-25.89
	PG 2303-1/4-3	14.44	95	0.17	1.19	-25.99
	PG 2303-1/5-1	13.74	63	0.18	0.78	-25.96
	PG 2303-1/5-3	14.37	93	0.17	1.16	-25.96
	PG 2303-1/6-3	16.10	103	0.14	1.28	-25.74
	PG 2303-7/0-1	14.02	58	0.18	0.72	-26.20
	PG 2303-7/1-2	13.02	56	0.20	0.70	-26.20
Lc 2	PG 2302-1/0-1	12.04	81	0.38	0.85	-26.60
	PG 2302-1/1-2	7.86	68	0.22	1.01	-26.20
Lc 3	PG 2305-1/0-1	12.98	57	0.20	0.70	-25.90
	PG 2305-1/1-2	13.08	56	0.20	0.70	-25.90
Lc 5	PG 2307-1/0-1	9.12	52	0.32	0.65	-26.40
	PG 2307-1/1-2	12.08	55	0.22	0.68	-26.40
Sc 7	PG 2308-1/0-1	9.40	54	0.31	0.67	-26.20
	PG 2308-1/1-2	9.80	53	0.30	0.66	-26.40
Sc 11	PG 2312-1/0-1	13.15	59	0.20	0.74	-25.90
	PG 2312-1/1-2	13.90	58	0.18	0.73	-25.90
Sc 12	PG 2313-1/0-1	11.88	56	0.23	0.70	-25.46
	PG 2313-1/1-2	13.11	56	0.20	0.70	-25.89
Sc 13	PG 2315-1/0-1	13.27	56	0.19	0.70	-26.20
	PG 2315-1/1-2	13.35	56	0.19	0.70	-26.20
Sc 14	PG 2316-1/0-1	11.42	54	0.24	0.67	-26.10
	PG 2316-1/1-2	13.16	57	0.19	0.71	-26.10
Sc 19	PG 2318-1/0-1	10.54	53	0.27	0.66	-26.20
	PG 2318-1/1-2	10.10	53	0.28	0.66	-26.20
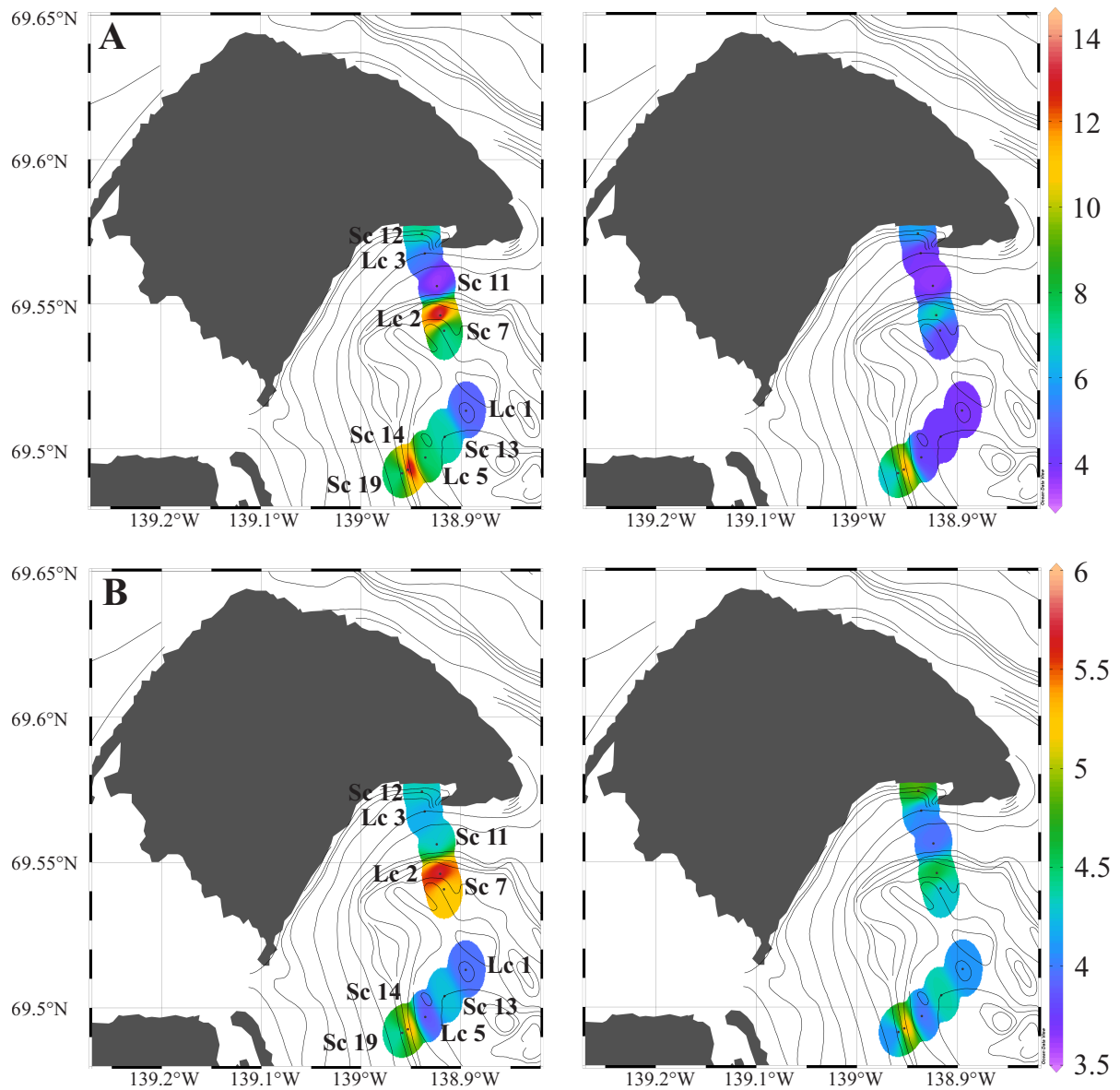
Fig. 4.3: A: Diploptene concentrations in ng/g TOC of all surface sediment samples. The image on the left shows the first centimetre of the surface samples, the image on the right-hand side the second centimetre respectively; B: CPI results of the surface sediment samples (left: first cm; right: second cm). Results shown in Fig. 4.3 A and B have been extrapolated for better comprehension
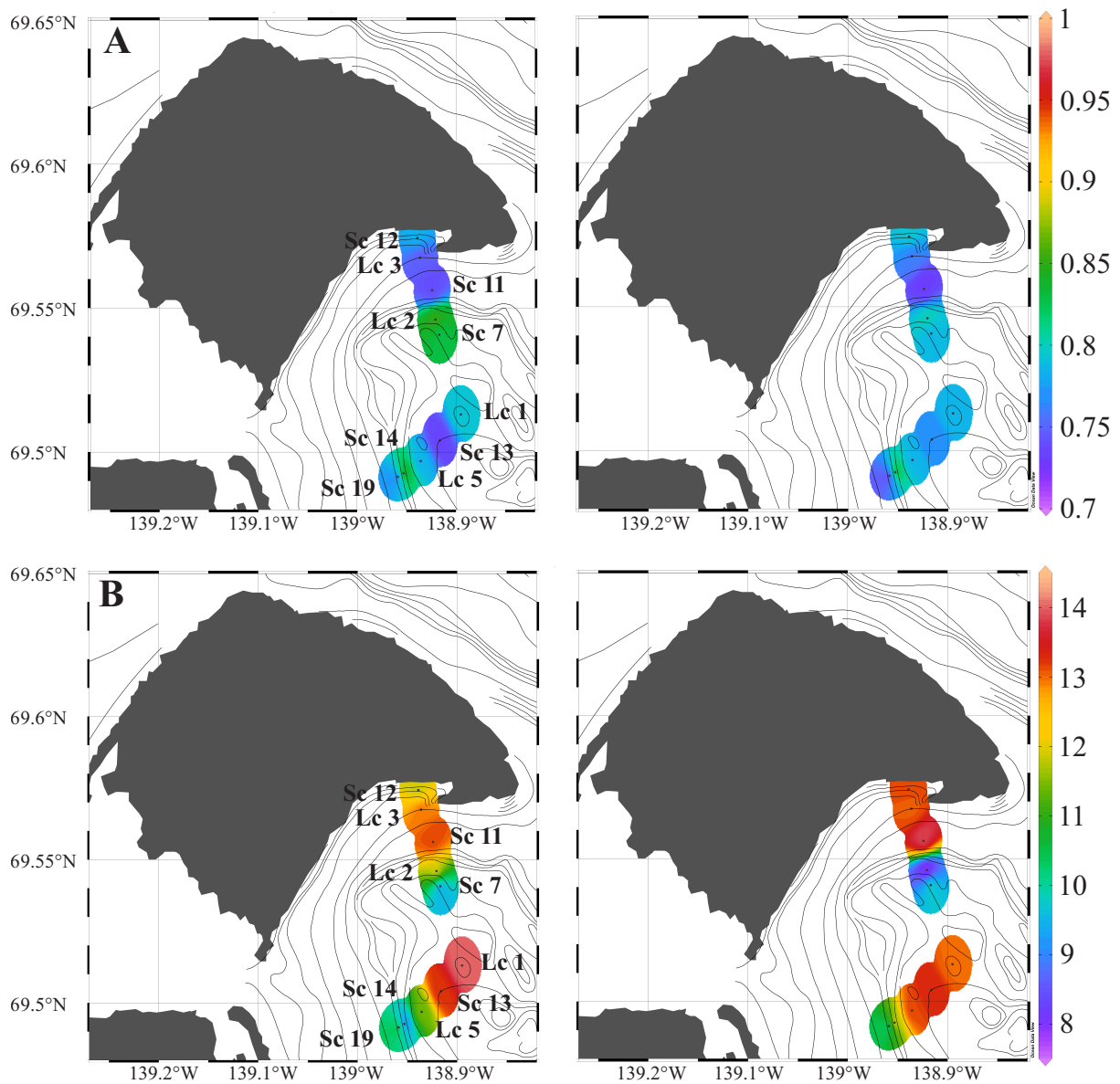
Fig. 4.4: A: BIT values of the surface sediment samples distributed over Herschel Basin (left: first cm; right: second cm); B: Radiocarbon ages of all surface sediments are illustrated in ka BP (left: first cm; right: second cm). Results shown in Fig. 4.4 A and B have been extrapolated for better comprehension

5. Discussion

The ratios and quantified results of the following sections were calculated with absolute values. Values given in the text and tables, as well as in the appendix, have been rounded for comprehensive reasons.

Samples from Komakuk Beach cannot be unambiguously distinguished from peat and SPM of the glaciated part of the YC, the Mackenzie River or from deposits on Herschel Island. Results of samples from the Komakuk Beach study site will therefore be neglected in the discussion. Sample SlpD15-PF-BIO01 will be preemptively excluded from further interpretations. Radiocarbon results of this sample exhibited a post-glacial value of 9.76 ka BP, which could have been caused through cryoturbation, but it is possible that the sample was confused during analysis or field work.

5.1. Biomarker signature of sediment contributors to Herschel Basin

The in Fig. 5.1 shown results are complemented with literature data from Yunker et al. (1992). The dataset comprises biomarker concentrations of SPM in the Mackenzie River Delta (Stn 1, Stn 0) and three samples from peat deposits along the glaciated YCP. Fig. 2.1 shows the sample locations of Stn 1 and Stn 0. Study sites of the three peat deposits are shown in Fig. 2.1. SPM samples of Stn 1 were retrieved during freshet of 1987 (April 11th, May 5th, May 30th) by the Institute of Ocean Sciences in British Columbia (Macdonald et al., 1988a; Macdonald et al., 1988b). Stn 0 was sampled at September 6th of the same year.

The dataset comprises hopanoid and *n*-alkane biomarker results (Table 5.1). GDGT concentrations are unfortunately missing in the dataset, as the samples were retrieved before these lipids gained the attention of the scientific community (Schouten et al., 2000; Sinninghe Damsté et al., 2000).

The relative composition of the diagenetic hopanes, $C_{29}17\alpha$, 21β-30-Norhopane and $C_{30}17\alpha$, 21β-Hopane, besides diploptene (17β, 21β-Hop-22(29)-ene) from the Mackenzie River Delta and peat deposits at King and Sabine Point is shown in Fig. 5.1. SPM data taken from Stn 1 sampled during freshet features high diploptene abundance and depletion of diagenetic hopanes. SPM data of Stn 0 sampled in September 1987 features an intermediate composition of these three hopanoid biomarkers. Results of the three peat deposits display a distinct predominance of diploptene.

Table 5.1: *n*-alkane and hopane biomarker data after Yunker et al. (1992). The data comprises Mackenzie River SPM and soil samples from three outcrops along the glaciated YCP

	Diploptene	29αβ	30αβ	CPI	C_{23}:C_{29} ratio	TAR
Mackenzie River SPM	[ng/l]	[ng/l]	[ng/l]			
Stn 1						
11th April	13.00	0.07	0.13	1.7	0.42	1.5
5th May	5.50	0.31	0.55	2.5	0.49	2.5
30th May	85.00	15.00	22.00	1.7	0.38	2.8
Stn 0						
6th September	30	10	23	2.4	0.48	1.3
peat samples	[ng/g]	[ng/g]	[ng/g]			
Sabine Pt.	12300	6.50	7.60	12.1	0.07	124.4
King/Sabine Pt.	5150	1070	37	9.1	0.22	18.4
King Pt.	36000	11		3.6	0.16	19.3

n-alkane results for samples derived from Yunker et al. (1992) are summarised in Table 5.1 and illustrated in Fig. 4.2. SPM from the Mackenzie River exhibit the lowest CPI and TAR values of all considered samples with a mean CPI of 2.1 and a mean TAR of 2.0. The mean value of the C_{23}:C_{29} ratio for these four SPM samples is 0.44, indicating a potential influence of *Sphagnum* derived *n*-alkanes through erosion of peat deposits within the drainage area of the Mackenzie River.

Samples from peat outcrops at King and Sabine Point display a high mean CPI of 8.3 and a high mean TAR of 54.0. Both indices display very high variance. The mean C_{23}:C_{29} ratio respectively shows a very low mean of 0.15. Peat deposits are not necessarily associated with high abundances of *Sphagnum* species. High abundance of odd long-chained alkanes in the observed peat deposits may indicate a primary gymnosperm plant source (Bush and McInerney, 2013) and relative absence of *Sphagnum* species, which would also explain high TAR ratios and relatively speaking low degradation of OM in these samples. Statements about the relative degree of degradation of a sample are only valid within the discussed dataset.

Samples shown in Fig. 5.1 align on a distinct trend determined by the relative abundance of both diagenetic hopanes and diploptene. The trend develops with decreasing abundance of diploptene and increasing abundance of both diagenetic hopanes, whereas $C_{29}17\alpha, 21\beta$-30-Norhopane shows a greater increase in abundance compared to $C_{30}17\alpha, 21\beta$-Hopane. According to Fig. 4.1 this trend shows a clear correlation with results of the Hopanoid-Index. With decreasing abundance of diploptene in contrast to the relative increase of both diagenetic hopanes, calculated values of the Hopanoid-Index decrease.
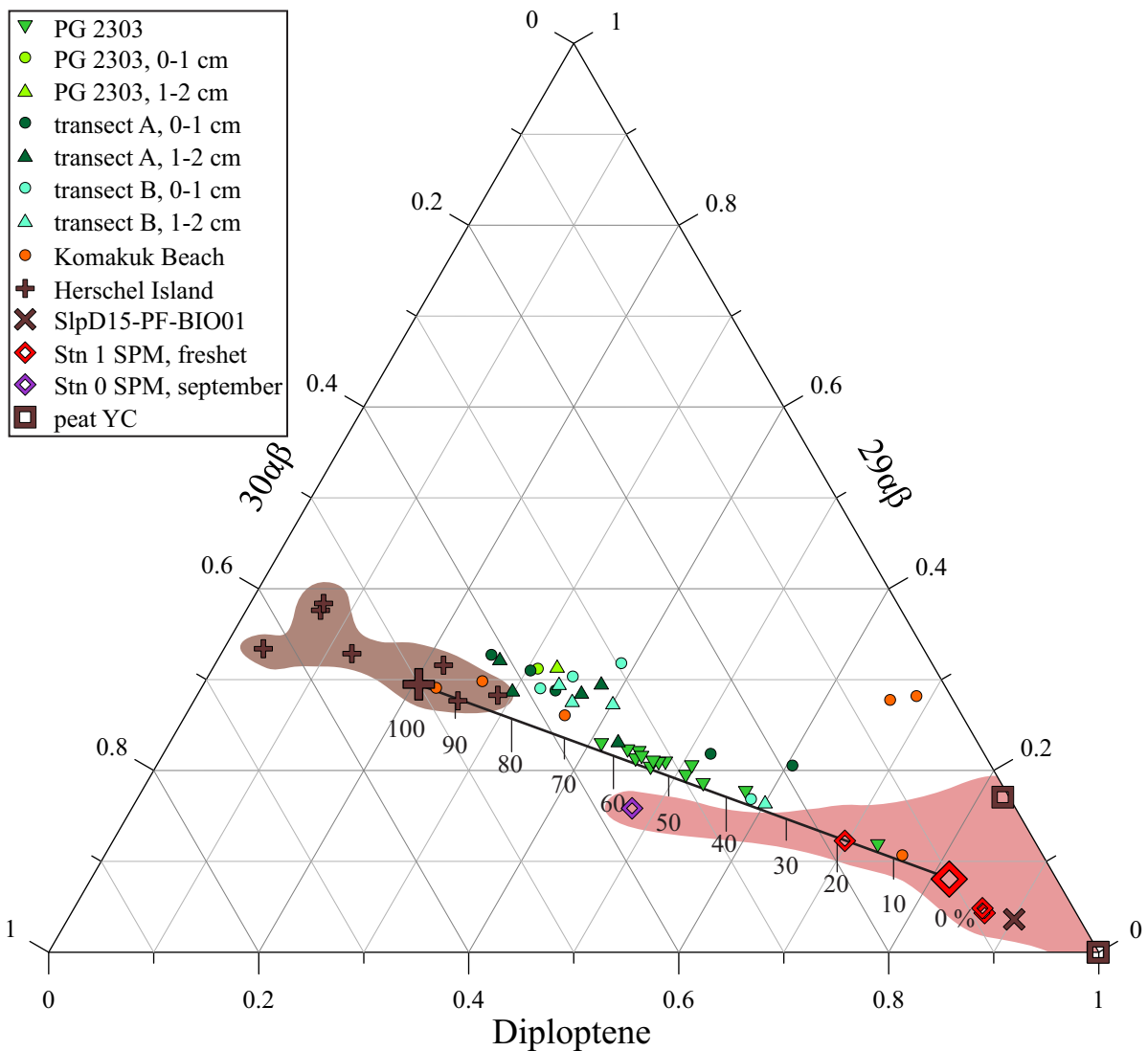
Fig. 5.1: Relative abundance between $C_{29}17\alpha$, 21β-30-Norhopane, $C_{30}17\alpha$, 21β-Hopane and diploptene (17β, 21β-Hop-22(29)-ene) of all analysed samples, SPM data from the Mackenzie River, and additional peat samples from the YCP located in between Herschel Island and the Mackenzie River (Yunker et al., 1992). The ternary plot features a linear regression between the Herschel and the Mackenzie endmember of the hopanoid endmember model. Brown and red plumes encompass the samples used for the calculation of each endmember. The scaling roughly suggests the sediment supply in Herschel Basin

Yunker et al. (1993) stated, that diploptene is mainly produced by bacterial production in peat deposits of the Mackenzie River catchment. As the Mackenzie River is the main contributor of sediment in the southern Beaufort Sea (Forbes, 1981), diploptene is assumed to be mostly supplied by SPM of the Mackenzie River. Yunker et al. (1993) reports high diploptene concentrations in SPM samples from the Mackenzie River retrieved before freshet. With increasing sediment load during freshet, Yunker et al. (1993) reported a decrease of diploptene

in analysed SPM. Samples collected on April 11th and May 5th 1987 show the highest relative abundance of diploptene , whereas SPM sampled in September of 1987 features a decrease of diploptene and a relative increase of petrogenic material (Fig. 5.1), presumably derived from the Devonian Canol formation (Yunker et al., 2002).

Findings from Yunker et al. (1993) are in accordance with the observed hopanoid distribution illustrated in Fig. 5.1. Except for SlpD15-PF-BIO01, samples from Herschel Island feature low diploptene to $C_{29}17\alpha$, 21β-30-Norhopane and $C_{30}17\alpha$, 21β-Hopane ratios and more advanced degradation (compare Fig. 4.1).

Fig. 5.3 features various saturate fraction chromatograms of samples from throughout the observed trend. UCM's visible in these *n*-alkane chromatograms show a coherence with the observed hopanoid distribution. Samples with a high relative abundance of diploptene clearly show no or only minor development of UCM's. Chromatograms with a high relative abundance of both diagenetic hopanes respectively show well developed UCM's instead. *n*-alkane chromatograms of all samples from Herschel Island, except of SlpD15-PF-BIO01, exhibit well developed UCM's.

These coherences distinctively display, that deposits from Herschel Island are the main contributors of degraded OC to Herschel Basin. Moreover, the state of degradation can be related to the radiocarbon age of each sample. The older the bulk organic matter of a sample is, the more distinct is its degradation. Samples presented in Fig. 5.2 show an overall increase in bulk radiocarbon age with decreasing abundance of diploptene.
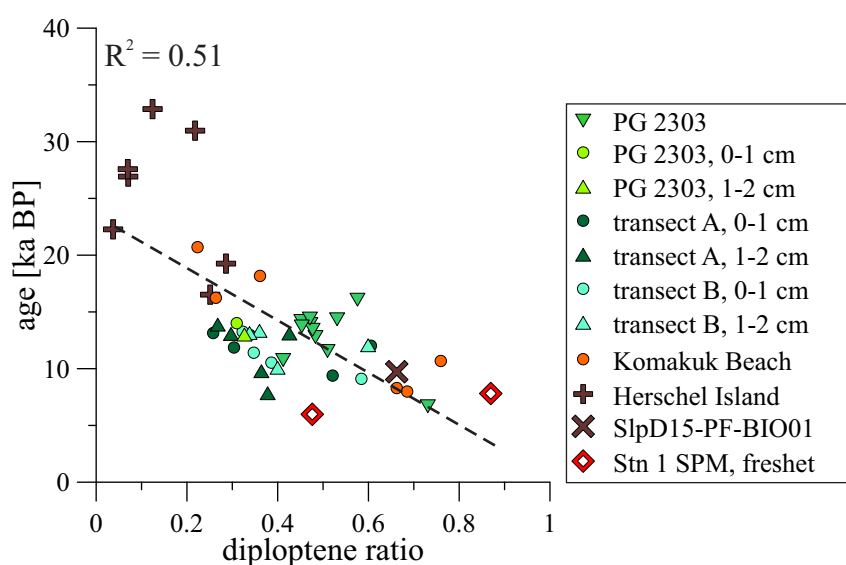
Fig. 5.2: Correlation of radiocarbon data and the diploptene ratio. The two red diamonds show combined literature data after Guo et al. (2007) and Yunker et al. (1992)

However, the distribution of associated CPI values, shown in Fig. 4.2, does not support this statement. CPI values of SPM from the Mackenzie River indicate a more degraded biomarker composition as deposits on Herschel Island and presumably strong petrogenic input or enhanced microbial production of short-chain *n*-alkanes (Choi and Lee, 2013; Yunker et al., 1993).
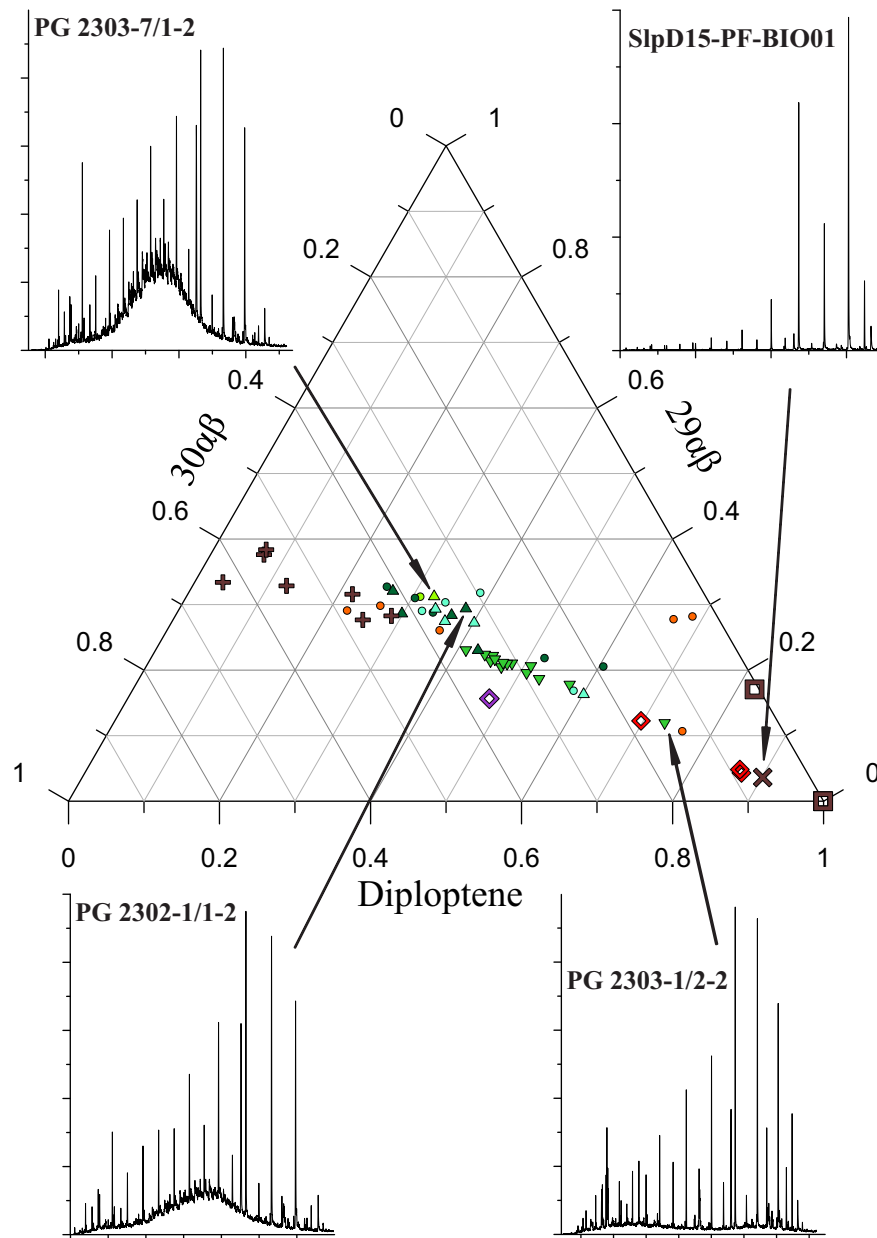
Fig. 5.3: UCM's observed in various saturate fraction chromatograms of soil and sediment samples from throughout the study area. The UCM's differ in development according to their relative state of degradation and location in the ternary diagram

5.2.   Spatial biomarker distribution in Herschel Basin

5.2.1.   Hopanoid endmember model
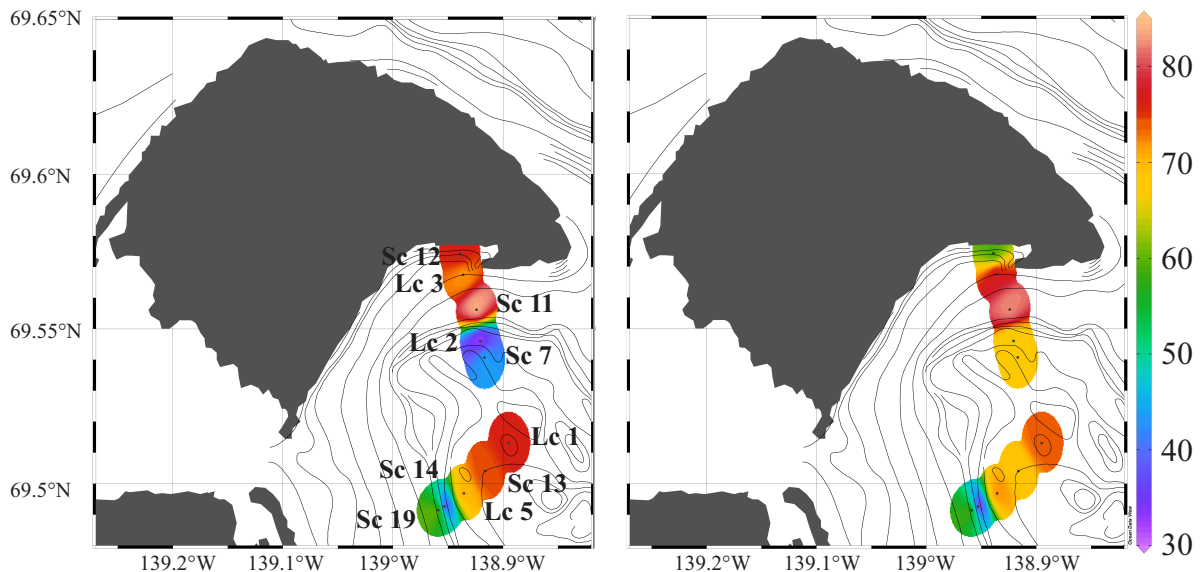
Fig. 5.4: Results of the hopanoid endmember model in % sediment supply by deposits of Herschel Island (left: first cm; right: second cm). Data points have been extrapolated for better comprehension

The relative composition of diploptene (17β, 21β-Hop-22(29)-ene) to C_{29}17α, 21β-30-Norhopane and C_{30}17α, 21β-Hopane investigated in all analysed samples and additional data taken after Yunker et al. (1992) features a distinct trend (Fig. 5.1).

To distinguish between various sediment input in Herschel Basin, a simple endmember model has been calculated. The model combines all four SPM samples of the Mackenzie River in combination with the three peat samples from the YCP and all samples from Herschel Island, with exception of SlpD15-PF-BIO01.

The relative sediment contribution of the Mackenzie River compared to the sediment supply by eroding coastal bluffs along the glaciated YCP and by smaller rivers like the Babbage River, can only be estimated. The endmember model is not capable of distinguishing between these different sources. Equally for sediment supply from the unglaciated part of the YCP (e.g. Komakuk Beach) westwards of Herschel Island. The contribution of marine produced OM could also not be distinguished with this endmember model. Results of the master thesis by Pfalz (2017) showed that OC in Herschel Basin is mostly derived from various terrigenous

sources. Consequently, the endmember model only distinguishes between sediment input from Herschel Island, the Mackenzie River and peat deposits along the YCP.

Values of the Herschel and the Mackenzie endmember were calculated as the mean ratio of diploptene versus $C_{29}\alpha\beta$ and $C_{30}\alpha\beta$ hopanes for all samples (diploptene/(diploptene + $C_{29}\alpha\beta$ + $C_{30}\alpha\beta$)). Values of all sediment samples were calculated the same way. Results of both endmembers (Herschel endmember = 0.15 (SD = 0.10); Mackenzie endmember = 0.82 (SD = 0.18)) were used for modelling a linear regression curve (Fig. 5.1). Results of the sediment samples are stated in percent relative to their proportional distribution on the constructed regression curve.

Results of the surface sediment samples calculated with the hopanoid endmember model are shown in Fig. 5.4 and are summarised in Table 5.4. 100 % meaning all hopanoid compounds are retrieved from deposits on Herschel Island, whereas 0 % means that all hopanoid compounds are supplied by the Mackenzie River and respectively from coastal peat deposits along the YCP. Endmember results of PG 2303 are listed in Table 5.2.

Table 5.2: Hopanoid endmember model results of PG 2303, calculated with the diploptene ratio

study site	sample ID	Hopanoid endmember model	% Herschel
Lc 1	PG 2303-1/2-1	0.41	61
	PG 2303-1/2-2	0.73	13
	PG 2303-1/3-1	0.51	46
	PG 2303-1/3-2	0.48	50
	PG 2303-1/3-3	0.47	52
	PG 2303-1/4-1	0.48	51
	PG 2303-1/4-2	0.45	55
	PG 2303-1/4-3	0.47	52
	PG 2303-1/5-1	0.45	55
	PG 2303-1/5-2	0.51	46
	PG 2303-1/5-3	0.53	43
	PG 2303-1/6-1	0.46	54
	PG 2303-1/6-2	0.44	57
	PG 2303-1/6-3	0.58	36

Ratios of diploptene to $C_{29}\alpha\beta$ and $C_{30}\alpha\beta$ show a correlation with the calculated results of the Hopanoid-Index (Fig. 4.1). As these hopanoid compounds make up most of the hopane

triterpenes in the samples from Herschel Island and as well in SPM of the Mackenzie River the endmember model can be used to characterize hopanoid derivation in Herschel Basin.

Fig. 5.4 shows the percental sediment distribution along transect A and transect B. As a general observation transect A shows overall a stronger contribution of the Herschel endmember as transect B. This can be recognized in both, the first and the second cm of the surface sediment samples. Transect B features a pattern of increasing values towards the basin centre in both maps. Samples from study sites (Sc 19, Lc 5) adjacent to the YCP clearly show hopanoid distributions with higher influence of the Mackenzie endmember. Transect A features a less distinctive pattern in its hopanoid distribution. Samples from the Sc 12, Lc 3 and Sc 11 coring locations feature a seemingly strong influence by eroded material from Herschel Island apart of one exception. Samples from the Lc 2 and Sc 7 coring locations show relatively high influence by the Mackenzie endmember in both maps. The reason, for transect A not showing a clear pattern of decreasing influence of the Herschel endmember with increasing distance to the Islands shore, is unclear. A possible explanation could be that the area of investigation is at a too small-scale to develop a distinct trend.

Overall, calculations of the hopanoid endmember model indicate a predominant influence of the Herschel endmember. The mean calculated value for all ten samples is 63 % for the first and 66 % for the second centimetre (Table 5.4).

Diploptene concentrations in the surface sediment samples coincide with findings by Yunker et al. (1993). Yunker et al. (1993) stated that most of the hopanoid biomarkers in the sediments of the Mackenzie Shelf are derived by SPM of the Mackenzie River, as long as SPM loadings remain at a high level. Investigations in Herschel Basin have shown, that hopane distribution in the sediments of the basin is clearly controlled by the sediment supply of the Mackenzie River supporting the statement of Yunker et al. (1993). Fig. 4.3 shows the absolute concentration of diploptene in each surface sediment sample. With stronger contribution by the Mackenzie endmember, diploptene concentrations feature a clear similar pattern and a relative increase.

The spatial distribution of *n*-alkanes in the surface sediment samples shows a similar pattern with results of the endmember model. Samples with higher CPI ratios (Fig. 4.2; CPI > 4.3) clearly feature a stronger influence of the Mackenzie endmember. Surface sediment samples showing a strong influence by the Herschel endmember display CPI values similar as the mean CPI value (3.41) of samples from Herschel Island. Similar observations coincide with the TAR

ratio and the endmember model, as the CPI and the TAR index display a direct correlation (Fig. 4.2). High TAR ratios coincide with enhanced influence of the Mackenzie endmember.

Surface sediment samples with a strong influence of the Mackenzie endmember exceed the mean CPI value of SPM from the Mackenzie River and rather resembles the values investigated in samples of King and Sabine Point. This leads to the conclusion, that erosion of coastal bluffs along the YCP might supply a significant amount of sediment to Herschel Basin. CPI results shown in Fig. 4.2 do not imply discharge of mature petroleum derived biomarkers into Herschel Basin. Curiale (1991) also stated the absence of biomarker input from petroleum reservoirs on the Mackenzie Shelf.

C_{23}:C_{29} ratios of all surface samples show no significant influence by *Sphagnum* enriched peat deposits. Moreover, analyses of peat deposits along the YCP (Yunker et al., 1992) revealed noticeable low C_{23}:C_{29} ratios. Coinciding with observed CPI and TAR distribution in the surface sediment samples from Herschel Basin (Fig. 4.2), low C_{23}:C_{29} ratios indicate significant sediment supply by coastal erosion along the glaciated YCP. Considering the relatively high C_{23}:C_{29} ratios in SPM of the Mackenzie River, coastal erosion of peat deposits along the glaciated YCP might be the prevailing portion of the Mackenzie endmember and as well the main driver for diploptene derivation in Herschel Basin.

Observed BIT distribution in the surface sediments of Herschel Basin (Fig. 4.4) resembles results of the hopanoid endmember model.

Surface sediment samples showing a strong resemblance with the Herschel endmember exhibit BIT values of about 0.75. These GDGT compositions may result from high abundance of crenarchaeol in some samples from Herschel Island, rather than by aquatic production of OM. The calculated BIT value of YC06-Col-2/26 is 0.51 and 0.75 for YC-Col-2/27 respectively. Bearing the geological history of the area in mind (paragraph 2.1.), it is likely that most of the crenarchaeol isoprenoid tetraether lipids in deposits on Herschel Island have an allochthonous origin. Using the BIT index to assess marine production of OM in Herschel Basin is therefore not possible.

Surface sediment samples with enhanced influence of the Mackenzie endmember display, relatively to the mean BIT value of all surface sediments (0.78), higher values. Thus, indicating a stronger terrigenous background typical for riverine SPM (De Jonge et al., 2015).

Minor contribution of marine OM to the BIT results of Herschel Basin cannot be assessed with GDGT data and needs further evaluation. Nevertheless, according to $\delta^{13}C$ and C/N results of

the master thesis by Pfalz (2017), marine OM only contributes with a small portion to the sediment budget of Herschel Basin.

The mean radiocarbon age of the seven samples, which were used to calculate the endmember of Herschel Island, is about 25 ka BP. Results of these samples feature pre-glacial and glacial radiocarbon ages and are in accordance with results by Fritz et al. (2012).
Radiocarbon values of riverine POC from the Mackenzie River indicate radiocarbon ages of 7.84 ka BP and 6.01 ka BP during the summer of 2004 (Table 5.3; Guo et al., 2007).
Radiocarbon results of the surface sediment samples are illustrated in Fig. 4.4. Investigated radiocarbon values reflect sediment supply by various sources and show a distinct similarity with the hopanoid endmember model (Fig. 5.1). Samples with relatively high radiocarbon values might indicate increased sediment supply by coastal erosion from Herschel Island. Conversely, samples with relatively young radiocarbon values can be attributed to enhanced sediment supply by SPM of the Mackenzie River.

Table 5.3: Radiocarbon data of POC from the Mackenzie River (Guo et al., 2007) and for Herschel Basin (Pfalz, 2017)

	^{14}C age [ka BP]	^{14}C error [± yr BP]	F^{14}C	F^{14}C error [%]	δ^{13}C [‰]
Mackenzie River POC					
22th June	7.84	50	0.38	0.62	-28.90
31th August	6.01	40	0.47	0.50	-26.79
"reservoir effect" Herschel Basin	1.10	100	0.87	1.24	-18 to -21

With accordance throughout *n*-alkane and GDGT biomarkers, as well as radiocarbon data of the surface sediment samples, the developed hopanoid endmember model can be considered as a rough estimation for the sediment supply in Herschel Basin and not just, as previously assumed, for hopanoid derivation. Hence, the hopanoid endmember model can be used to quantify OC input of various sources to the sediment budget of Herschel Basin.

5.2.2.   F^{14}C endmember model

A second endmember model has been compiled to confirm findings of the hopanoid endmember model, or, if differences occur, to discuss the possible origin of such.

The F^{14}C endmember model was established with δ^{13}C and with F^{14}C data. It consists of an endmember representing permafrost deposits on Herschel Island, one representing SPM derived through the Mackenzie River and an endmember for marine POC (Fig. 5.5). As bulk org. radiocarbon values of the surface sediment samples show a comparable distribution with the hopanoid endmember model, similar results of the F^{14}C endmember model are to be expected.
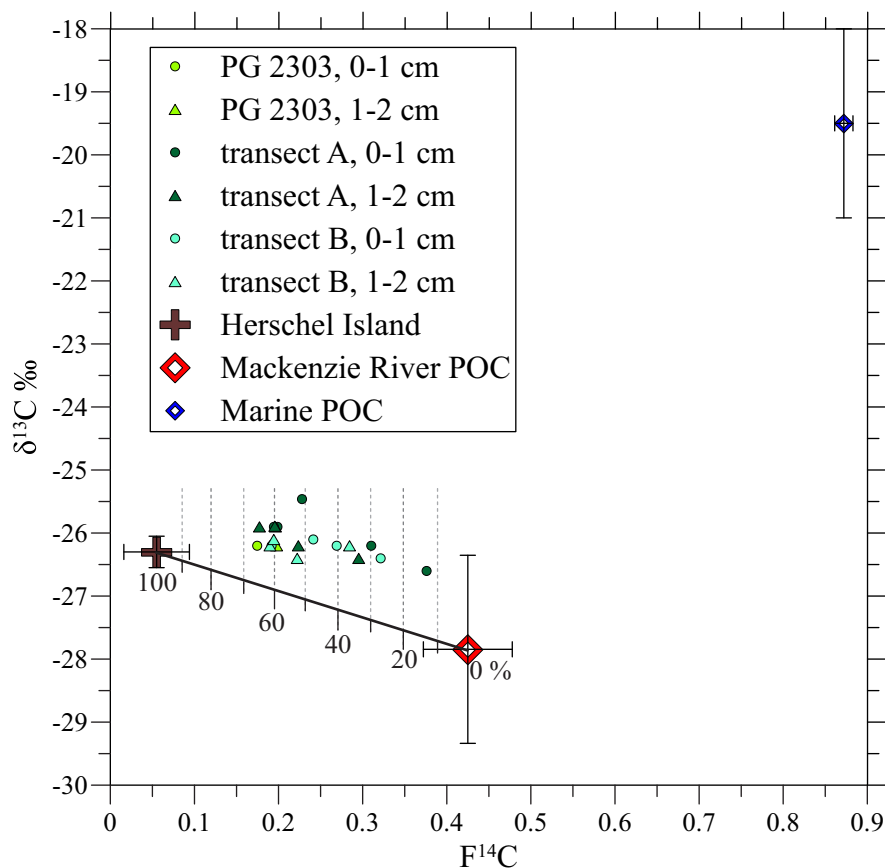
Fig. 5.5: The F^{14}C endmember model. The marine POC endmember (blue diamond) and the F^{14}C Mackenzie endmember (red diamond) combine data from the literature (Guo et al., 2007; Lamb et al., 2006; Pfalz, 2017; Yunker et al., 1992). F^{14}C endmember results of the surface sediments are based on the linear regression between the F^{14}C Mackenzie and the F^{14}C Herschel endmember. The scaling represents correct values, as calculations have been accomplished two-dimensional under exclusion of the marine POC endmember

The calculation for the $F^{14}C$ endmember of Herschel Island is based on the same seven samples, which were used for the hopanoid endmember model. $F^{14}C$ values for the mentioned samples descending from Herschel Island are given in Table 4.1. The $F^{14}C$ Mackenzie endmember consists of POC radiocarbon data from the Mackenzie River. Two samples were included from Guo et al. (2007). The samples were taken on the 22th June and the 31th August 2004, about 200 km upstream the Mackenzie River (67.46°N; 133.62°W) close to the community Tsiigehtchic (Table 5.3). The marine POC endmember was determined with the estimated reservoir effect of 1.1 ka BP for sediments in Herschel Basin, defined by Pfalz (2017) and $\delta^{13}C$ by Lamb et al. (2006). According to Lamb et al. (2006) typical $\delta^{13}C$ values of marine POC range between -18 ‰ and -21 ‰. $F^{14}C$ values of the marine and the $F^{14}C$ Mackenzie endmember are given in Table 5.3.
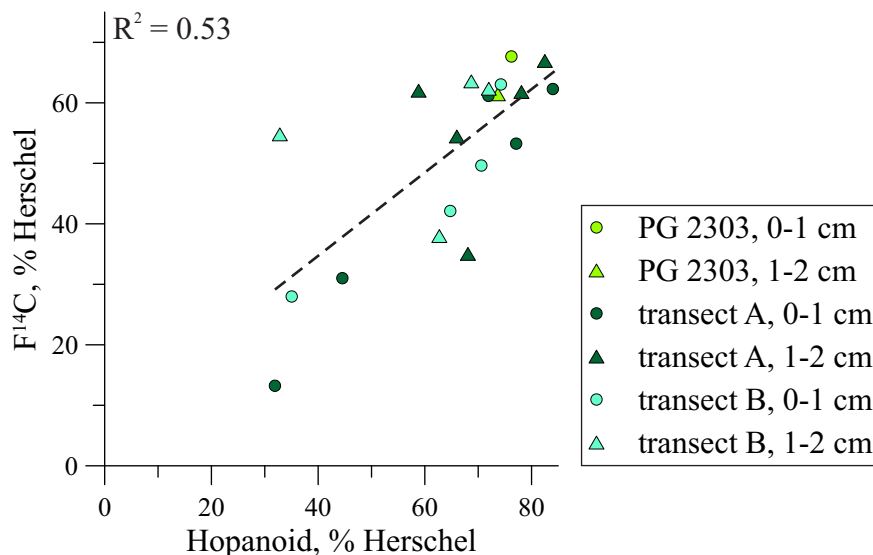
Fig. 5.6: Correlation of results calculated with both endmember models. The values, stated in percent, indicate sediment supply by eroded OM from Herschel Island

Distribution of the surface sediment samples shown in Fig. 5.5 exhibit strong influence by the $F^{14}C$ Herschel and the $F^{14}C$ Mackenzie endmember. Influence of the marine POC endmember is barely visible. $\delta^{13}C$ and C/N results discussed by Pfalz (2017) clearly show that marine algae and phytoplankton only contribute a small amount to sediments in Herschel Basin. Results of the $F^{14}C$ endmember model have been calculated as two-dimensional model with negligence of the marine POC endmember. Averaged $F^{14}C$ values of the $F^{14}C$ Herschel endmember ($F^{14}C$ mean = 0.06; SD = 0.04) and the $F^{14}C$ Mackenzie endmember ($F^{14}C$ mean = 0.43; SD = 0.07) have been used to model a linear regression curve. Results of the surface sediment samples

were calculated like associated samples of the hopanoid endmember model and are stated in percent as well. Further quantification will also be conducted under negligence of the marine POC endmember.

The calculated results of the $F^{14}C$ endmember model are given in Table 5.4. The mean value for the upper centimetre of all ten surface sediment samples shows that 47 % of the sediment at these sample locations is supplied by deposits from Herschel Island. The respective result, expressed in % sediment supply by deposits of Herschel Island, for the second centimetre is 56 %. Both values indicate a more balanced sediment supply of the $F^{14}C$ Herschel and the $F^{14}C$ Mackenzie endmember as associated results calculated with the hopanoid endmember model. Due to unavailability of radiocarbon data, samples from the glaciated YCP could not be represented in this endmember model.

As a result, the $F^{14}C$ endmember model only distinguishes between two sources of terrigenous OC – OC derived from Herschel Island and from the Mackenzie River. Expectably, results of this endmember model are presumptively less accurate as results of the hopanoid endmember model. Nevertheless, results of both independent endmember models show a surprisingly good correlation. Fig. 5.6 shows the resemblance of both endmember models in percental sediment supply by deposits from Herschel Island.

Table 5.4: Summary of the hopanoid and the $F^{14}C$ endmember model for all surface sediments

study site	sample ID	Hopanoid endmember model	% Herschel	$F^{14}C$ endmember model	% Herschel
Lc 1	PG 2303-7/0-1	0.31	76	0.18	68
	PG 2303-7/1-2	0.33	74	0.20	62
Lc 2	PG 2302-1/0-1	0.61	32	0.38	13
	PG 2302-1/1-2	0.38	66	0.22	55
Lc 3	PG 2305-1/0-1	0.34	72	0.20	61
	PG 2305-1/1-2	0.30	78	0.20	62
Lc 5	PG 2307-1/0-1	0.58	35	0.32	28
	PG 2307-1/1-2	0.60	33	0.22	55
Sc 7	PG 2308-1/0-1	0.52	44	0.31	31
	PG 2308-1/1-2	0.36	68	0.30	35
Sc 11	PG 2312-1/0-1	0.26	84	0.20	62
	PG 2312-1/1-2	0.27	83	0.18	67
Sc 12	PG 2313-1/0-1	0.30	77	0.23	53
	PG 2313-1/1-2	0.43	59	0.20	62
Sc 13	PG 2315-1/0-1	0.32	74	0.19	63
	PG 2315-1/1-2	0.36	69	0.19	64
Sc 14	PG 2316-1/0-1	0.35	71	0.24	50
	PG 2316-1/1-2	0.34	72	0.19	62
Sc 19	PG 2318-1/0-1	0.39	65	0.27	42
	PG 2318-1/1-2	0.40	63	0.28	38

5.3. Quantification of OM from Herschel Island

To quantify the amount of coastally eroded material from Herschel Island in the sediments of Herschel Basin, the sediment budget calculated by Pfalz (2017) was used. Pfalz (2017) calculated an average annual sedimentation rate of 0.33 cm/a for Herschel Basin. The average annual sediment deposition in Herschel Basin equals 720,000 tons, calculated with an averaged sediment density of 1,700 kg/m^3 and a surface area of Herschel Basin of 127,000,000 m^2. Assuming an average TOC content of 1.83 %, about 13,200 tons of OC will be deposited within Herschel Basin every year (Pfalz, 2017).

Since the study sites Lc 3, Sc 11 and Sc 12 (Fig. 2.2) are not located within Herschel Basin, samples from these locations were not included in the final quantification of sediment supply in Herschel Basin. Also, as samples from the remaining seven study sites roughly cover a third of the surface area of Herschel Basin, I assume that 1/3 of the sediment budget of Herschel Basin can be quantified with results of the surface samples taken from the Lc 1, Lc 2, Lc 5, Sc7, Sc 13, Sc 14 and Sc 19 study sites. 1/3 of the surface area of Herschel Basin equals an average sediment budget of 240,000 tons and 4,400 tons of OC every year.

Quantifications for both endmember models combine the first and the second cm of all surface sediment samples from the remaining seven study sites (Table 5.4). The mean percental value calculated with results of the hopanoid endmember model is 60 %. The corresponding value calculated with the F^{14}C endmember model is 47 %. Overall, results of the hopanoid endmember model exceed those of the F^{14}C endmember model. Calculated values are given in Table 5.5. According to the quantification of the hopanoid endmember model each year approximately 144,000 tons (2640 t/a of OC) of sediments from Herschel Island are deposited within the upper third of Herschel Basin. The associated value calculated with the F^{14}C endmember model is 114,000 tons (2090 t/a of OC) of sediment every year.

Table 5.6: Quantified results of sediments in Herschel Basin with origin of coastal erosion on Herschel Island

	Hopanoid endmember model	F^{14}C endmember model
sediment supply [Mt/a]	0.144	0.114
[m^3/a]	84792	66985
OC supply [t/a]	2640	2090

Calculations of both individual endmember models feature surprisingly similar results. Though, both endmember models contain various causes for potential uncertainty.

Uncertainties may emerge as both endmember models are only based on seven samples from TSD and TSD, which is not enough to assess the heterogeneity of deposits from Herschel Island. The same holds true for the determination of the Mackenzie endmember and the $F^{14}C$ Mackenzie endmember.

Future quantifications should consider determining between different depositional environments of Herschel Island. For instance, to separate between the basin centre and the periphery of Herschel Basin. These realms seem to host varying biomarker compositions, implying different sediment transport mechanisms yet unknown. With a higher sampling density, it would also be possible to estimate the sediment budget on the Yukon Coastal Shelf and the nearshore area around Herschel Island, among obtaining a higher resolution within Herschel Basin itself.

However, the quantifications of the sedimentary budget of Herschel Basin, considering similar outcome of both individual endmember models, seems to be a valid first approach.

5.4. Temporal changes of sedimentation
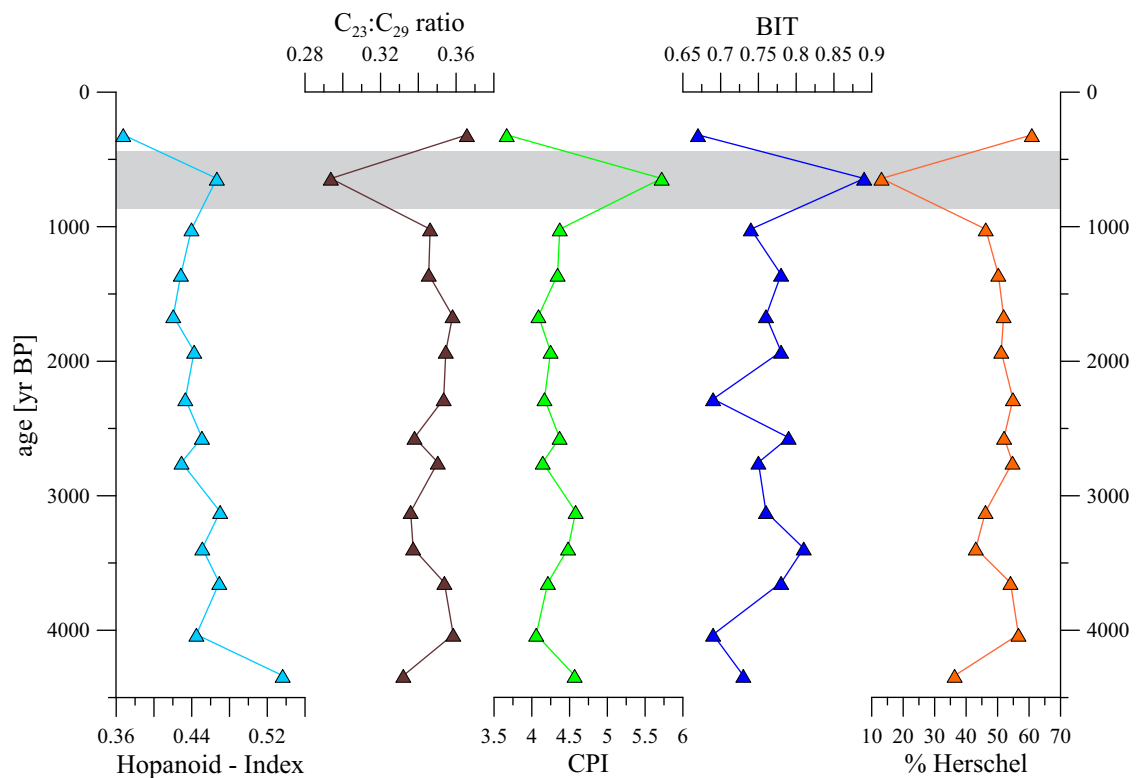
Fig. 5.7: Hopane, *n*-alkane, GDGT and hopanoid endmember results of PG 2303 samples. The grey rectangle indicates a climate anomaly at approximately 650 yr BP

Biomarker results and results of the hopanoid endmember model for PG 2303 are summarised in Fig. 5.7. The hopanoid endmember model can roughly be used to quantify the sediment supply of Herschel Basin, assuming if sediment input by the Mackenzie River did not change essentially over the last 4 ka BP. Results of the hopanoid endmember model indicate a more or less stagnating distribution throughout most of the sediment core with a mean result of 48 %. With 76 % (PG 2303-7/0-1) and 74 % (PG 2303-7/1-2), associated results of both surface sediment samples from the same study site indicate an enhanced sediment supply by deposits from Herschel Island. Coinciding findings are also indicated in all biomarker indices and radiocarbon results.

The highlighted area in Fig. 5.7 shows an anomaly at about 650 yr BP. The abrupt change is visible in all indicated data and suggests enhanced sediment supply by the Mackenzie River or the YCP. According to the hopanoid endmember model only 13 % of the respective sediment sample from study site Lc 1 is derived from Herschel Island. This anomaly is followed by a steep gap suggesting increased erosion of deposits from Herschel Island. Increased sediment supply by the Mackenzie River could be induced through a period of cooler climatic conditions. The study by O'Brien et al. (1995) reported on several climate periodicities during the Holocene corresponding with glacier advances in the St. Elias Mountains (southern Yukon Territory; Denton and Karlén, 1973). The most recent event corresponded with the timing of the Little Ice Age (LIA; ca. 1400 − 1850 AD; Campbell et al., 1998). Poor correspondence of the observed anomaly in PG 2303 and the timing of the LIA might be related to the estimated error of the reservoir age (± 100 yr), or to inaccuracy of the age-depth model. It is likewise possible, that the change in sedimentation has been caused by a regional climate event.

6.   Conclusion

The first question, if biomarker compositions could aid to distinguish between different sources of sediment deposited in Herschel Basin could partially be validated.

Investigations on the hopanoid composition of sediments from Herschel Island concluded in very distinct findings. The hopanoid distribution of these deposits indicated minor occurrence of diploptene, which is mostly derived from bacterial production in peat deposits (Yunker et al., 1993). In this unique geological setting, diploptene is mostly derived from SPM of the Mackenzie River or coastal bluffs along the glaciated part of the YCP (Yunker et al., 1993). Sediments from the Komakuk Beach study site displayed a wide range of biomarker variability and could not be unambiguously distinguished from other sediment sources.

The second question, regarding distinguishing OM input from various sources into Herschel Basin, was answered with the depiction of two individual endmember models. With both endmember models, different sediment sources in Herschel Basin could be distinguished, albeit contrasting findings between *n*-alkanes and hopanoid biomarkers. Both endmember models resulted in comparable findings.

According to Hill et al. (1991), 95 % of the total sediment supply to the Mackenzie Shelf is contributed by SPM of the Mackenzie River. The biomarker composition of the surface sediment samples, however, suggested strong supply of eroded deposits from Herschel Island in Herschel Basin. Speaking for the northwestern area of Herschel Basin, coastally eroded material from Herschel Island represents the dominant sediment source. This dominance is even more distinct in the shallow nearshore zone at the east coast of Herschel Island.

Hopanoid and *n*-alkane compositions further suggested high sediment contribution of coastal bluffs along the glaciated YCP in contrast to SPM supply by the Mackenzie River. Separating between the individual proportion of OM derived from the Mackenzie River and the glaciated YCP was however not possible.

The minor contribution of marine OM in Herschel Basin could not be assessed. By including additional biomarker data, it could be possible to detect a compound of clear recent marine origin in the surface sediments of Herschel Basin.

The main objective, of quantifying OM derived from deposits on Herschel Island in the sediments of Herschel Basin, was achieved. Findings of this thesis support the hypothesis stated in the master thesis of Pfalz (2017), that large amounts of OC are removed from the Arctic carbon cycle by reburial in Herschel Basin.

A detailed description, of the sedimentary change in Herschel Basin over the past 4 ka BP, was impeded by the poor resolution of PG 2303. Albeit, analyses on the sediment core resulted in the following conclusions. The biomarker composition in PG 2303 suggested an overall consistent sedimentation until approximately 1.00 ka BP. Between 1.00 to 0.65 ka BP the data suggests the beginning of a short cold period, which may be of regional or global extent. Quantifications with the hopanoid endmember model indicated enhanced riverine sediment supply during this period. Assignment to a specific climate event was not possible. Subsequently, endmember modelling on samples from the Lc 1 study site indicate increased sediment supply by deposits from Herschel Island from 0.65 ka BP until today, presumably induced by enhanced coastal erosion.

Outlook

For further assessment of the sedimentation in Herschel Basin, additional data should be consulted.

Via coastal parallel currents (Pelletier et al., 1984) unknown amounts of SPM are guided through "Workboat Passage". SPM samples from "Workboat Passage" at mainly westerly winds could help to distinguish and quantify OC derived from coastal bluffs along Komakuk Beach. Moreover, including SPM data from smaller rivers, adjacent to Herschel Basin, would be beneficial. A more detailed reconstruction of the climatic variability and the anthropogenic effect in the southern Beaufort Sea could be obtained through additional analyses of PG 2303 and the associated gravity core. Especially a high resolution in the upper metre of PG 2303 would increase understanding of the anthropogenic impact on the carbon cycle in the southern Beaufort Sea. Concluding, further assessment on the heterogeneity of deposits on Herschel Island, by including additional samples from retrogressive thaw slumps, would improve the accuracy of future quantifications of the sedimentation in Herschel Basin.

The data discussed in this thesis is archived in the Open Access library PANGAEA (www.Pangaea.de).

7. Acknowledgement

8. References

Abbott, G.D., Zahra Bashir, F., Sugden, M.A., 2001. Kerogen-bound and free hopanoic acids in the Messel oil shale kerogen. *Chirality 13*, 510–516. doi:10.1002/chir.1069

AMAP, 2012. Arctic Climate Issues 2011: Changes in Arctic Snow, Water, Ice and Permafrost. *SWIPA 2011 Overview Report. Arctic Monitoring and Assessment Programme (AMAP)*, Oslo. xi + 97pp.

Anisimov, O.A., Vaughan, D.G., Callaghan, T. V, Furgal, C., Marchant, H., Prowse, T.D., Vilhjálmsson, H., Walsh, J.E., 2007. Polar regions (Arctic and Antarctic), in: Parry, M.L., Canziani, O.F., Palutikof, J.P., van der Linden, P.J., Hanson, C.E. (Eds.), *Climate Change 2007: Impacts, Adaptation and Vulnerability. Contribution of Working Group II to the Fourth Assessment Report of the Intergovernmental Panel on Climate Change*. Cambridge University Press, Cambridge, pp. 653–685.

Bailey, N.J.L., Jobson, A.M., Rogers, M.A., 1973. Bacterial degradation of crude oil: comparison of field and experimental data. *Chemical Geology 11*, 203–221.

Bird, M.I., Summons, R.E., Gagan, M.K., Roksandic, Z., Dowling, L., Head, J., Fifield, L.K., Cresswell, R.G., Johnson, D.P., 1995. Terrestrial vegetation change inferred from n-alkane $\delta^{13}C$ analysis in the marine environment. *Geochimica et Cosmochimica Acta 59*, 2853–2857. doi:http://dx.doi.org/10.1016/0016-7037(95)00160-2

Bost, F.D., Frontera-Suau, R., McDonald, T.J., Peters, K.E., Morris, P.J., 2001. Aerobic biodegradation of hopanes and norhopanes in Venezuelan crude oils. *Organic Geochemistry 32*, 105–114. doi:10.1016/S0146-6380(00)00147-9
Bouchard, M., 1974. Surficial geology of Herschel Island, Yukon territory. University of Montreal.

Bourbonniere, R.A., Meyers, P.A., 1996. Sedimentary geolipid records of historical changes in the watersheds and productivities of Lakes Ontario and Erie. *Limnology and Oceanography 41*, 352–359. doi:10.4319/lo.1996.41.2.0352

Bray, E.E., Evans, E.D., 1961. Distribution of n-paraffins as a clue to recognition of source beds. *Geochimica et Cosmochimica Acta 22*, 2–15. doi:10.1016/0016-7037(61)90069-2

Brown, R.J.E., Kupsch, W.O., 1974. Permafrost terminology. *National Research Council of Canada Technical*, 62 pp.

Burn, C.R., 2009. After whom is Herschel Island named? *Arctic 62*, 317–323.

Burn, C.R., Zhang, Y., 2009. Permafrost and climate change at Herschel Island (Qikiqtaruq), Yukon Territory, Canada. *Journal of Geophysical Research 114*, 1–16. doi:10.1029/2008JF001087

Bush, R.T., McInerney, F.A., 2013. Leaf wax *n*-alkane distributions in and across modern plants: Implications for paleoecology and chemotaxonomy. *Geochimica et Cosmochimica Acta 117*, 161–179. doi:10.1016/j.gca.2013.04.016

Campbell, I.D., Campbell, C., Apps, M.J., Rutter, N.W., Bush, A.B.G., 1998. Late Holocene ~1500 yr climatic periodicities and their implications. *Geology 26*, 471–473. doi:10.1130/0091-7613(1998)026<0471:LHYCPA>2.3.CO;2

Carmack, E.C., Macdonald, R.W., 2002. Oceanography of the Canadian shelf of the Beaufort Sea: A setting for marine life. *Arctic 55*, 29–45. doi:10.1126/science.100.2596.291

Carrie, J., Sanei, H., Goodarzi, F., Stern, G., Wang, F., 2009. Characterization of organic matter in surface sediments of the Mackenzie River Basin, Canada. *International Journal of Coal Geology 77*, 416–423. doi:10.1016/j.coal.2008.03.007

Carson, M.A., Jasper, J.N., Conly, P.M., 1998. Magnitude and sources of sediment input to the Mackenzie Delta, Northwest Territories, 1974-94. *Arctic 51*, 116–124.

Castañeda, I.S., Schouten, S., 2011. A review of molecular organic proxies for examining modern and ancient lacustrine environments. *Quaternary Science Reviews 30*, 2851–2891. doi:10.1016/j.quascirev.2011.07.009

Chibnall, A.C., Piper, S.H., Pollard, A., Williams, E.F., Sahai, P.N., 1934. The constitution of the primary alcohols, fatty acids and paraffins present in plant and insect waxes. *Biogeochemistry 28*, 2189–2208.

Choi, Y.J., Lee, S.Y., 2013. Microbial production of short-chain alkanes. *Nature 502*, 571–574. doi:10.1038/nature12536

Cooper, J.E., Bray, E.E., 1963. A postulated role of fatty acids in petroleum formation. *Geochimica et Cosmochimica Acta 27*, 1113–1127. doi:10.1016/0016-7037(63)90093-0

Couture, N., 2010. *Fluxes of soil organic carbon from eroding permafrost coasts, Canadian Beaufort Sea*. McGill University, Montreal.

Cranwell, P.A., Eglinton, G., Robinson, N., 1987. Lipids of aquatic organisms as potential contributors to lacustrine sediments–II*. *Organic Geochemistry 11*, 513–527. doi:10.1016/0146-6380(87)90007-6

Curiale, J.A., 1991. The petroleum geochemistry of Canadian Beaufort Tertiary "non-marine" oils. *Chemical Geology 93*, 21–45. doi:10.1016/0009-2541(91)90062-V

Davidson, E.A., Janssens, I.A., 2006. Temperature sensitivity of soil carbon decomposition and feedbacks to climate change. *Nature 440*, 165–73. doi:10.1038/nature04514

De Jonge, C., Stadnitskaia, A., Hopmans, E.C., Cherkashov, G., Fedotov, A., Streletskaya, I.D., Vasiliev, A.A., Sinninghe Damsté, J.S., 2015. Drastic changes in the distribution of branched tetraether lipids in suspended matter and sediments from the Yenisei River and Kara Sea (Siberia): Implications for the use of brGDGT-based proxies in coastal marine sediments. *Geochimica et Cosmochimica Acta 165*, 200–225. doi:10.1016/j.gca.2015.05.044

de Krom, V., 1990. *A geomorphic investigation of retrogressive thaw slumps and active layer slides on Herschel Island, Yukon Territory*. McGill University, Montreal.

De Rosa, M., Gambacorta, A., 1988. The lipids of archaebacteria. *Prog. Lipid Res. 27*, 153–175.

Denton, G.H., Karlén, W., 1973. Holocene climatic variations–their pattern and possible cause. *Quaternary Research 3*, 155–205. doi:10.1016/0033-5894(73)90040-9

Dyke, A.S., Prest, V.K., 1987. Late Wisconsinan and Holocene History of the Laurentide Ice Sheet. *Géographie physique et Quaternaire 41*, 237. doi:10.7202/032681ar

Eglinton, G., Hamilton, R.J., 1967. Leaf epicuticular waxes. *Science (New York, N.Y.) 156*, 1322–1335. doi:10.1126/science.156.3780.1322

Eglinton, G., Logan, G.A., 1991. Molecular preservation. *Phil. Trans. R. Soc. Lond. B 333*, 315–328. doi:10.1098/rstb.1991.0081

Ficken, K.J., Li, B., Swain, D.L., Eglinton, G., 2000. An *n*-alkane proxy for the sedimentary input of submerged/floating freshwater aquatic macrophytes. *Organic Geochemistry 31*, 745–749. doi:10.1016/S0146-6380(00)00081-4

Forbes, D.L., 1981. *Babbage River delta and lagoon: hydrology and sedimentology of an Arctic estuarine system*. University of Toronto. doi:10.14288/1.0095397

Fritz, M., Vonk, J.E., Lantuit, H., 2017. Collapsing Arctic coastlines. *Nature Climate Change 7*, 6–7. doi:10.1038/nclimate3188

Fritz, M., Wetterich, S., Meyer, H., Schirrmeister, L., Lantuit, H., Pollard, W.H., 2011. Origin and characteristics of massive ground ice on Herschel Island (Western Canadian Arctic) as revealed by stable water isotope and hydrochemical signatures. *Permafrost and Periglacial Processes 22*, 26–38. doi:10.1002/ppp.714

Fritz, M., Wetterich, S., Schirrmeister, L., Meyer, H., Lantuit, H., Preusser, F., Pollard, W.H., 2012. Eastern Beringia and beyond: Late Wisconsinan and Holocene landscape dynamics along the Yukon Coastal Plain, Canada. *Palaeogeography, Palaeoclimatology, Palaeoecology 319–320*, 28–45. doi:10.1016/j.palaeo.2011.12.015

Gough, M.A., Rhead, M.M., Rowland, S.J., 1992. Biodegradation studies of unresolved complex mixtures of hydrocarbons: model UCM hydrocarbons and the aliphatic UCM. *Organic Geochemistry 18*, 17–22. doi:10.1016/0146-6380(92)90139-O

Gruber, N., Friedlingstein, P., Field, C.B., Valentini, R., Heimann, M., Richey, J.E., Lankao, P.R., Schulze, E.-D., Chen, C.-T.A., 2004. The vulnerability of the carbon cycle in the 21st century: An assessment of carbon-climate-human interactions, in: Field, C.B., Raupach, M.R. (Eds.), *The Global Carbon Cycle: Integrating Humans, Climate, and the Natural World*. Island Press, Washington D.C, Washington D.C., pp. 45–76.

Gruber, S., 2012. Derivation and analysis of a high-resolution estimate of global permafrost zonation. *The Cryosphere 6*, 221–233. doi:10.5194/tc-6-221-2012

Guo, L., Ping, C.L., Macdonald, R.W., 2007. Mobilization pathways of organic carbon from permafrost to Arctic rivers in a changing climate. *Geophysical Research Letters 34*, 1–5. doi:10.1029/2007GL030689

Harper, J.R., 1990. Morphology of the Canadian Beaufort Sea coast. *Marine Geology 91*, 75–91. doi:10.1016/0025-3227(90)90134-6

Hill, P.R., Blasco, S.M., Harper, J.R., Fissel, D.B., 1991. Sedimentation on the Canadian Beaufort Shelf. *Continental Shelf Research 11*, 821–842. doi:10.1016/0278-4343(91)90081-G

Hill, P.R., Mudie, P.J., Moran, K., Blasco, S.M., 1985. A sea-level curve for the Canadian Beaufort Shelf. *Canadian Journal of Earth Sciences 22*, 1383–1393. doi:10.1139/e85-146

Holmes, R.M., McClelland, J.W., Peterson, B.J., Tank, S.E., Bulygina, E., Eglinton, T.I., Gordeev, V. V., Gurtovaya, T.Y., Raymond, P.A., Repeta, D.J., Staples, R., Striegl, R.G., Zhulidov, A. V., Zimov, S.A., 2012. Seasonal and Annual Fluxes of Nutrients and Organic Matter from Large Rivers to the Arctic Ocean and Surrounding Seas. *Estuaries and Coasts 35*, 369–382. doi:10.1007/s12237-011-9386-6

Hopmans, E.C., Schouten, S., Pancost, R.D., Van Der Meer, M.T.J., Sinninghe Damsté, J.S., 2000. Analysis of intact tetraether lipids in archaeal cell material and sediments by high performance liquid chromatography/atmospheric pressure chemical ionization mass spectrometry. *Rapid Communications in Mass Spectrometry 14*, 585–589. doi:10.1002/(SICI)1097-0231(20000415)14:7<585::AID-RCM913>3.0.CO;2-N

Hopmans, E.C., Weijers, J.W.H., Schefuß, E., Herfort, L., Sinninghe Damsté, J.S., Schouten, S., 2004. A novel proxy for terrestrial organic matter in sediments based on branched and isoprenoid tetraether lipids. *Earth and Planetary Science Letters 275*, 107–116.

Huggett, W.S., Woodward, M.J., Stephenson, F., Hermiston, F. V, Douglas, A., 1975. Near bottom currents and offshore tides. *Beaufort Sea Technical Report Nr. 16*. Geological Survey of Canada.

IPCC, 2007. Climate Change 2007 Synthesis Report, Synthesis Report. Contribution of Working Groups I, II and III to the Fourth Assessment Report of the Intergovernmental Panel on Climate Change [Core Writing Team, Pachauri, R.K. and Reisinger, A. (Eds.)]. *IPCC*. Geneva. Switzerland. 104 pp. doi:10.1256/004316502320517344

Jeng, W.L., 2006. Higher plant *n*-alkane average chain length as an indicator of petrogenic hydrocarbon contamination in marine sediments. *Marine Chemistry 102*, 242–251. doi:10.1016/j.marchem.2006.05.001

Kattsov, V.M., Källén, E., 2005. Future Climate Change: Modeling and Scenarios for the Arctic, in: Symon, C., Arris, L., Heal, B. (Eds.), *Arctic Climate Impact Assessment (ACIA)*. Cambridge University Press, New York, pp. 99–150.

Kirner, D.L., Taylor, R.E., Southon, J.R., 1995. Reduction in backgrounds of microsamples for AMS ^{14}C dating. *Radiocarbon 37*, 697–704.

Lamb, A.L., Wilson, G.P., Leng, M.J., 2006. A review of coastal palaeoclimate and relative sea-level reconstructions using $\delta^{13}C$ and C/N ratios in organic material. *Earth-Science Reviews 75*, 29–57. doi:10.1016/j.earscirev.2005.10.003

Lantuit, H., Overduin, P.P., Couture, N., Wetterich, S., Aré, F., Atkinson, D., Brown, J., Cherkashov, G., Drozdov, D., Forbes, D.L., Graves-Gaylord, A., Grigoriev, M., Hubberten, H.W., Jordan, J., Jorgenson, T., Ødegård, R.S., Ogorodov, S., Pollard, W.H., Rachold, V., Sedenko, S., Solomon, S., Steenhuisen, F., Streletskaya, I., Vasiliev, A., 2012a. The Arctic Coastal Dynamics Database: A New Classification Scheme and Statistics on Arctic Permafrost Coastlines. *Estuaries and Coasts 35*, 383–400. doi:10.1007/s12237-010-9362-6

Lantuit, H., Pollard, W.H., 2005. Temporal stereophotogrammetric analysis of retrogressive thaw slumps on Herschel Island, Yukon Territory. *Natural Hazards and Earth System Science 5*, 413–423. doi:10.5194/nhess-5-413-2005

Lantuit, H., Pollard, W.H., 2008. Fifty years of coastal erosion and retrogressive thaw slump activity on Herschel Island, southern Beaufort Sea, Yukon Territory, Canada. *Geomorphology 95*, 84–102. doi:10.1016/j.geomorph.2006.07.040

Lantuit, H., Pollard, W.H., Couture, N., Fritz, M., Schirrmeister, L., Meyer, H., Hubberten, H.W., 2012b. Modern and Late Holocene retrogressive thaw slump activity on the Yukon Coastal Plain and Herschel Island, Yukon Territory, Canada. *Permafrost and Periglacial Processes 23*, 39–51. doi:10.1002/ppp.1731

Lantz, T.C., Kokelj, S. V, 2008. Increasing rates of retrogressive thaw slump activity in the Mackenzie Delta region, N.W.T., Canada. *Geophysical Research Letters 35*, 1–5. doi:10.1029/2007GL032433

Lewis, C.P., Forbes, D.L., 1975. Coastal sedimentary processes and sediments, southern Beaufort Sea. *Beaufort Sea Technical Report Nr. 24*. Geological Survey of Canada.

Lichtfouse, É., Derenne, S., Mariotti, A., Largeau, C., 1994. Possible algal origin of long chain odd *n*-alkanes in immature sediments as revealed by distributions and carbon isotope ratios. *Organic Geochemistry 22*, 1023–1027. doi:10.1016/0146-6380(94)90035-3

Macdonald, R.W., Iseki, K., O'Brien, M.C., McLaughlin, F.A., McCullough, D., MacDonald, D.M., Carmack, E.C., Adams, H., Yunker, M., Buckingham, S., 1988. NOGAP B.6; Volume 4: Chemical data collected in the Beaufort Sea. Summer 1987. *Can. Data Rep. Hydrogr. Ocean Sci 60*, 1–115.

Macdonald, R.W., Iseki, K., O'Brien, M.C., McLaughlin, F.A., McCullough, D., MacDonald, D.M., Carmack, E.C., Yunker, M., Buckingham, S., Miskulin, G., 1988. NOGAP B.6; Volume 5: Chemical data collected in the Beaufort Sea and Mackenzie River Delta, March-July 1987. *Can. Data Rep. Hydrogr. Ocean Sci 60*, 1–65.

Macdonald, R.W., Solomon, S.M., Cranston, R.E., Welch, H.E., Yunker, M.B., Gobeil, C., 1998. A sediment and organic carbon budget for the Canadian Beaufort Shelf. *Marine Geology 144*, 255–273. doi:10.1016/S0025-3227(97)00106-0

Mackay, J.R., 1959. Glacier ice-thrust features of the Yukon Coast. *Geographical Bulletin 13*, 5–21.

Mackay, J.R., 1971. The Origin of Massive Icy Beds in Permafrost, Western Arctic Coast, Canada. *Canadian Journal of Earth Sciences 8*, 807–817. doi:10.1038/2031227a0

Marzi, R., Torkelson, B.E., Olson, R.K., 1993. A revised carbon preference index. *Organic Geochemistry 20*, 1303–1306. doi:10.1016/0146-6380(93)90016-5

Mead, R., Xu, Y., Chong, J., Jaffé, R., 2005. Sediment and soil organic matter source assessment as revealed by the molecular distribution and carbon isotopic composition of *n*-alkanes. *Organic Geochemistry 36*, 363–370. doi:10.1016/j.orggeochem.2004.10.003

Meehl, G.A., Stocker, T.F., Collins, W.D., Friedlingstein, P., Gaye, A.T., Gregory, J.M., Kitoh, A., Knutti, R., Murphy, J.M., Noda, A., Raper, S.C.B., Watterson, I.G., Weaver, A.J., Zhao, Z.-C., 2007. Global Climate Projections, in: Solomon, S., Qin, D., Manning, M., Chen, Z., Marquis, M., Averyt, K.B., Tignor, M., Miller, H.L. (Eds.), *Climate Change 2007: The Physical Science Basis. Contribution of Working Group I to the Fourth Assessment Report of the Intergovernmental Panel on Climate Change*. Cambridge University Press, Cambridge, pp. 747–846. doi:10.1080/07341510601092191

Meyer, V.D., Max, L., Hefter, J., Tiedemann, R., Mollenhauer, G., 2016. Glacial-to-Holocene evolution of sea surface temperature and surface circulation in the subarctic northwest Pacific and the Western Bering Sea. *Paleoceanography 31*, 916–927. doi:10.1002/2015PA002877

Mollenhauer, G., Basse, A., Kim, J.H., Sinninghe Damsté, J.S., Fischer, G., 2015. A four-year record of U$^K_{37}$- and TEX$_{86}$-derived sea surface temperature estimates from sinking particles in the filamentous upwelling region off Cape Blanc, Mauritania. *Deep-Sea Research Part I: Oceanographic Research Papers 97*, 67–79. doi:10.1016/j.dsr.2014.11.015

Nichols, J.E., Booth, R.K., Jackson, S.T., Pendall, E.G., Huang, Y., 2006. Paleohydrologic reconstruction based on *n*-alkane distributions in ombrotrophic peat. *Organic Geochemistry 37*, 1505–1513. doi:10.1016/j.orggeochem.2006.06.020

Nievas, M.L., Commendatore, M.G., Esteves, J.L., Bucalá, V., 2008. Biodegradation pattern of hydrocarbons from a fuel oil-type complex residue by an emulsifier-producing microbial consortium. *Journal of Hazardous Materials 154*, 96–104. doi:10.1016/j.jhazmat.2007.09.112

Nott, C.J., Xie, S., Avsejs, L.A., Maddy, D., Chambers, F.M., Evershed, R.P., 2000. *n*-Alkane distributions in ombrotrophic mires as indicators of vegetation change related to climatic variation. *Organic Geochemistry 31*, 231–235. doi:10.1016/S0146-6380(99)00153-9

O'Brien, S.R., Mayewski, P.A., Meeker, L.D., Meese, D.A., Twickler, M.S., Whitlow, S.I., 1995. Complexity of Holocene climate as reconstructed from a Greenland ice core. *Science 270*, 1962–1964. doi:DOI 10.1126/science.270.5244.1962

O'Connor, M.J., 1984. *Surficial geology and granular resources southeast of Herschel Island*.

Obu, J., Lantuit, H., Fritz, M., Pollard, W.H., Sachs, T., Günther, F., 2016. Relation between planimetric and volumetric measurements of permafrost coast erosion: a case study from Herschel Island, western Canadian Arctic. *Polar Research 35*, 1–13. doi:10.3402/polar.v35.30313

Ochsenreiter, T., Selezi, D., Quaiser, A., Bonch-Osmolovskaya, L., Schleper, C., 2003. Diversity and abundance of Crenarchaeota in terrestrial habitats studied by 16S RNA surveys and real time PCR. *Environmental Microbiology 5*, 787–797. doi:10.1046/j.1462-2920.2003.00476.x

Olynyk, M., 2008. Summary of the significance of and threats to cultural resources located at the historic settlement area on Herschel Island territorial park of Yukon, in: Petzet, M., Ziesemer, J. (Eds.), *Heritage at Risk: ICOMOS World Report 2006/2007 on Monuments and Sites in Danger*. Reinhold-Verlag, pp. 212–214.

Pancost, R.D., Baas, M., van Geel, B., Sinninghe Damsté, J.S., 2002. Biomarkers as proxies for plant inputs to peats: an example from a sub-boreal ombrotrophic bog. *Organic Geochemistry 33*, 675–690. doi:10.1016/S0146-6380(02)00048-7

Pelletier, B.R., Bornhold, B.D.B., Buckley, D.E., Costaschuk, S., Forbes, D.L., Lewis, C.F.M., Matsumoto, E., Meagher, L., Walker, D.A., Wong, C.S., 1984. Marine Science Atlas of the Beaufort Sea – Sediment. *Geological Survey of Canada*.

Peters, K.E., Walters, C.C., Moldowan, J.M., 2005. *The Biomarker Guide, Volume 1*. Cambridge University Press.

Pfalz, G., 2017. *Lateral transport of sediment and organic matter, derived from coastal erosion, into the nearshore zone of the southern Beaufort Sea, Canada*. Technische Universität Dresden.

Philippi, G.T., 1977. On the depth, time and mechanism of origin of the heavy to medium-gravity naphthenic crude oils. *Geochimica et Cosmochimica Acta 41*, 33–52. doi:10.1016/0016-7037(77)90185-5

Pollard, W., 1990. The nature and origin of ground ice in the Herschel Island area, Yukon Territory. *Proceedings of the fifth Canadian Conference on Permafrost*, 23–30.

Powers, L.A., Werne, J.P., Johnson, T.C., Hopmans, E.C., Sinninghe Damsté, J.S., Schouten, S., 2004. Crenarchaeotal membrane lipids in lake sediments: A new paleotemperature proxy for continental paleoclimate reconstruction? *Geology 32*, 613–616. doi:10.1130/G20434.1

Radosavljevic, B., Lantuit, H., Pollard, W., Overduin, P., Couture, N., Sachs, T., Helm, V., Fritz, M., 2015. Erosion and flooding—threats to coastal infrastructure in the Arctic: a case study from Herschel Island, Yukon Territory, Canada. *Estuaries and Coasts*. doi:10.1007/s12237-015-0046-0

Rampton, V.N., 1982. Quaternary Geology of the Yukon Coastal Plain. *Geological Survey of Canada*, Open File 1144.

Reed, W.E., 1977. Molecular compositions of weathered petroleum and comparison with its possible source. *Geochimica et Cosmochimica Acta 41*, 237–247. doi:10.1016/0016-7037(77)90231-9

Reimer, P.J., Brown, T.A., Reimer, R.W., 2004. Discussion: Reporting and calibration of post-bomb ^{14}C data. *Radiocarbon 46*, 1299–1304.

Requejo, A.G., Halpern, H.I., 1989. An unusual hopane biodegradation sequence in tar sands from the Pt Arena (Monterey) Formation. *Nature 342*, 670–673. doi:doi:10.1038/342670a0

Sachse, D., Radke, J., Gleixner, G., 2004. Hydrogen isotope ratios of recent lacustrine sedimentary *n*-alkanes record modern climate variability. *Geochimica et Cosmochimica Acta 68*, 4877–4889. doi:10.1016/j.gca.2004.06.004

Sakata, S., Hayes, J.M., Rohmer, M., Hooper, A.B., Seemann, M., 2008. Stable carbon-isotopic compositions of lipids isolated from the ammonia-oxidizing chemoautotroph *Nitrosomonas europaea*. *Organic Geochemistry 39*, 1725–1734. doi:10.1016/j.orggeochem.2008.08.005

Schefuß, E., Ratmeyer, V., Stuut, J.B.W., Jansen, J.H.F., Sinninghe Damsté, J.S., 2003. Carbon isotope analyses of n-alkanes in dust from the lower atmosphere over the central eastern Atlantic. *Geochimica et Cosmochimica Acta 67*, 1757–1767. doi:10.1016/s0016-7037(02)01414-x

Schouten, S., Forster, A., Panoto, F.E., Sinninghe Damsté, J.S., 2007a. Towards calibration of the TEX$_{86}$ palaeothermometer for tropical sea surface temperature in ancient greenhouse worlds. *Organic Geochemistry 38*, 1537–1546. doi:10.1029/2004PA001041

Schouten, S., Hopmans, E.C., Pancost, R.D., Sinninghe Damsté, J.S., 2000. Widespread occurrence of structurally diverse tetraether membrane lipids: Evidence for the ubiquitous presence of low-temperature relatives of hyperthermophiles. *PNAS 97*, 14421–14426. doi:10.1073/pnas.97.26.14421

Schouten, S., Hopmans, E.C., Sinninghe Damsté, J.S., 2013. The organic geochemistry of glycerol dialkyl glycerol tetraether lipids: A review. *Organic Geochemistry 54*, 19–61. doi:10.1016/j.orggeochem.2012.09.006

Schouten, S., van der Meer, M.T.J., Hopmans, E.C., Rijpstra, W.I.C., Reysenbach, A.L., Ward, D.M., Sinninghe Damsté, J.S., 2007b. Archaeal and bacterial glycerol dialkyl glycerol tetraether lipids in hot springs of Yellowstone National Park. *Applied and Environmental Microbiology 73*, 6181–6191. doi:10.1128/AEM.00630-07

Schuur, E.A.G., Bockheim, J., Canadell, J.G., Euskirchen, E., Field, C.B., Goryachkin, S. V., Hagemann, S., Kuhry, P., Lafleur, P.M., Lee, H., Mazhitova, G., Nelson, F.E., Rinke, A., Romanovsky, V.E., Shiklomanov, N., Tarnocai, C., Venevsky, S., Vogel, J.G., Zimov, S.A., 2008. Vulnerability of permafrost carbon to climate change: implications for the global carbon cycle. *BioScience 58*, 701–714.

Schuur, E.A.G., McGuire, A.D., Schädel, C., Grosse, G., Harden, J.W., Hayes, D.J., Hugelius, G., Koven, C.D., Kuhry, P., Lawrence, D.M., Natali, S.M., Olefeldt, D., Romanovsky, V.E., Schaefer, K., Turetsky, M.R., Treat, C.C., Vonk, J.E., 2015. Climate change and the permafrost carbon feedback. *Nature 520*, 171–179. doi:10.1038/nature14338

Seifert, W.K., Moldowan, M.J., 1978. Applications of steranes, terpanes and monoaromatics to the maturation, migration and source of crude oils. *Geochimica et Cosmochimica Acta 42*, 77–95. doi:10.1016/0016-7037(78)90219-3

Simoneit, B.R.T., 1977. Organic matter in eolian dusts over the Atlantic Ocean. *Marine Chemistry 5*, 443–464.

Simoneit, B.R.T., 1984. Organic matter of the troposphere-III. Characterization and sources of petroleum and pyrogenic residues in aerosols over the western United States. *Atmospheric Environment 18*, 51–67. doi:10.1016/0004-6981(84)90228-2

Sinninghe Damsté, J.S., Hopmans, E.C., Pancost, R.D., Schouten, S., Geenevasen, J.A.J., 2000. Newly discovered non-isoprenoid glycerol dialkyl glycerol tetraether lipids in sediments. *Chemical Communications*. 1683–1684. doi:10.1039/b004517i

Sinninghe Damsté, J.S., Schouten, S., Hopmans, E.C., van Duin, A.C.T., Geenevasen, J.A.J., 2002. Crenarchaeol: the characteristic core glycerol dibiphytanyl glycerol tetraether membrane lipid of cosmopolitan pelagic crenarchaeota. *The Journal of Lipid Research 43*, 1641–1651. doi:10.1194/jlr.M200148-JLR200

Smith, S., Burgess, M., 2000. Ground temperature database for Northern Canada. *Geological Survey of Canada Open File Report 3954*, 57pp.

Snowdon, L.R., Stasiuk, L.D., Robinson, R., Dixon, J., Dietrich, J., McNeil, D.H., 2004. Organic geochemistry and organic petrology of a potential source rock of early Eocene age in the Beaufort-Mackenzie Basin. *Organic Geochemistry 35*, 1039–1052. doi:10.1016/j.orggeochem.2004.04.006

Streletskiy, D., Anisimov, O., Vasiliev, A., 2014. Permafrost Degradation, in: Shroder, J., Haeberli, W., Whiteman, C. (Eds.), *Snow and Ice-Related Hazards, Risks, and Disasters*. Elsevier Inc., pp. 303–344. doi:10.1016/B978-0-12-394849-6.00010-X

Stuiver, M., Polach, H.A., 1977. Discussion: Reporting of ^{14}C data. *Radiocarbon 19*, 355–363.

Synal, H.A., Stocker, M., Suter, M., 2007. MICADAS: A new compact radiocarbon AMS system. *Nuclear Instruments and Methods in Physics Research, Section B: Beam Interactions with Materials and Atoms 259*, 7–13. doi:10.1016/j.nimb.2007.01.138

Tarnocai, C., Canadell, J.G., Schuur, E.A.G., Kuhry, P., Mazhitova, G., Zimov, S., 2009. Soil organic carbon pools in the northern circumpolar permafrost region. *Global Biogeochemical Cycles 23*, 1–11. doi:10.1029/2008GB003327

van Dongen, B.E., Semiletov, I., Weijers, J.W.H., Gustafsson, Ö., 2008. Contrasting lipid biomarker composition of terrestrial organic matter exported from across the Eurasian Arctic by the five great Russian Arctic rivers. *Global Biogeochemical Cycles 22*, 1–14. doi:10.1029/2007GB002974

Van Everdingen, R. (ed.), 1998. *Multi-language glossary of permafrost and related ground-ice terms*. Revised May 2005. National Snow and Ice Data Center/World Data Center for Glaciology. Boulder. CO. http://nsidc.org/fgdc/glossary/.

Volkman, J.K., Alexander, R., Kagi, R.I., Woodhouse, G.W., 1983. Demethylated hopanes in crude oils and their applications in petroleum geochemistry. *Geochimica et Cosmochimica Acta 47*, 785–794. doi:10.1016/0016-7037(83)90112-6

Vonk, J.E., Giosan, L., Blusztajn, J., Montlucon, D., Graf Pannatier, E., McIntyre, C., Wacker, L., Macdonald, R.W., Yunker, M.B., Eglinton, T.I., 2015. Spatial variations in geochemical characteristics of the modern Mackenzie Delta sedimentary system. *Geochimica et Cosmochimica Acta 171*, 100–120. doi:10.1016/j.gca.2015.08.005

Vonk, J.E., Gustafsson, Ö., 2009. Calibrating *n*-alkane *Sphagnum* proxies in sub-Arctic Scandinavia. *Organic Geochemistry 40*, 1085–1090. doi:10.1016/j.orggeochem.2009.07.002

Vonk, J.E., Gustafsson, Ö., 2013. Permafrost-carbon complexities. *Nature Geoscience 6*, 675–676. doi:10.1038/ngeo1937

Wacker, L., Christl, M., Synal, H.A., 2010a. Bats: A new tool for AMS data reduction. *Nuclear Instruments and Methods in Physics Research B 268*, 976–979. doi:10.1016/j.nimb.2009.10.078

Wacker, L., Němec, M., Bourquin, J., 2010b. A revolutionary graphitisation system: Fully automated, compact and simple. *Nuclear Instruments and Methods in Physics Research, Section B 268*, 931–934. doi:10.1016/j.nimb.2009.10.067

Wagner, B., 2003. The Expeditions Amery Oasis, East Antarctica, in 2001/02 and Taylor Valley, Southern Victoria Land, in 2002. *Ber. Polarforsch. Meeresforsch 460*, 80.

Wardroper, A.M.K., Hoffmann, C.F., Maxwell, J.R., Barwise, A.J.G., Goodwin, N.S., Park, P.J.D., 1984. Crude oil biodegradation under simulated and natural conditions–II. Aromatic steroid hydrocarbons. *Organic Geochemistry 6*, 605–617. doi:10.1016/0146-6380(84)90083-4

Weijers, J.W.H., Blaga, C.I., Werne, J.P., Sinninghe Damsté, J.S., 2009. Microbial membrane lipids in lake sediments as a paleothermometer. *PAGES news 17*, 102–105.

Weijers, J.W.H., Schouten, S., Hopmans, E.C., Geenevasen, J.A.J., David, O.R.P., Coleman, J.M., Pancost, R.D., Sinninghe Damsté, J.S., 2006a. Membrane lipids of mesophilic anaerobic bacteria thriving in peats have typical archaeal traits. *Environmental Microbiology 8*, 648–657. doi:10.1111/j.1462-2920.2005.00941.x

Weijers, J.W.H., Schouten, S., Spaargaren, O.C., Sinninghe Damsté, J.S., 2006b. Occurrence and distribution of tetraether membrane lipids in soils: Implications for the use of the TEX$_{86}$ proxy and the BIT index. *Organic Geochemistry 37*, 1680–1693. doi:10.1016/j.orggeochem.2006.07.018

Weijers, J.W.H., Schouten, S., van der Linden, M., van Geel, B., Sinninghe Damsté, J.S., 2004. Water table related variations in the abundance of intact archaeal membrane lipids in a Swedish peat bog. *FEMS Microbiology Letters 239*, 51–56. doi:10.1016/j.femsle.2004.08.012

Wenger, L.M., Isaksen, G.H., 2002. Control of hydrocarbon seepage intensity on level of biodegradation in sea bottom sediments. *Organic Geochemistry 33*, 1277–1292. doi:10.1016/S0146-6380(02)00116-X

Winterfeld, M., Goñi, M.A., Just, J., Hefter, J., Mollenhauer, G., 2015. Characterization of particulate organic matter in the Lena River delta and adjacent nearshore zone, NE Siberia – Part 2: Lignin-derived phenol compositions. *Biogeosciences 12*, 2261–2283. doi:10.5194/bg-12-2261-2015

Yunker, M.B., Backus, S.M., Graf Pannatier, E., Jeffries, D.S., Macdonald, R.W., 2002. Sources and significance of alkane and PAH hydrocarbons in Canadian Arctic rivers. *Estuarine Coastal and Shelf Science 55*, 1–31. doi:10.1006/ecss.2001.0880

Yunker, M.B., Macdonald, R.W., Cretney, W.J., Fowler, B.R., McLaughlin, F.A., 1993. Alkane, terpene, and polycyclic aromatic hydrocarbon geochemistry of the Mackenzie River and Mackenzie shelf: Riverine contributions to Beaufort Sea coastal sediment. *Geochim. Cosmochim. Acta 57*, 3041–3061.

Yunker, M.B., McLaughlin, F.A., Fowler, B.R., Brooks, G., Chiddell, G., Hamilton, C., Macdonald, R.W., 1992. NOGAP B.6; Volume 9: Hydrocarbon determinations; Mackenzie River and Beaufort Sea. *Can. Data Rep. Hydrogr. Ocean Sci. 9*, 1–294.